The Astrophysical Journal, 929:94 (19pp), 2022 April 10 https://doi.org/10.3847/1538-4357/ac5d3a

Quenching and the *UVJ* Diagram in the SIMBA Cosmological Simulation

Hollis B. Akins[1], Desika Narayanan[2,3,4], Katherine E. Whitaker[4,5], Romeel Davé[6,7,8], Sidney Lower[2], Rachel Bezanson[9], Robert Feldmann[10], and Mariska Kriek[11]
[1] Department of Physics, Grinnell College, 1116 Eighth Ave., Grinnell, IA 50112, USA; hollis.akins@gmail.com
[2] Department of Astronomy, University of Florida, 211 Bryant Space Sciences Center, Gainesville, FL 32611, USA
[3] University of Florida Informatics Institute, 432 Newell Drive, CISE Bldg. E251, Gainesville, FL 32611, USA
[4] Cosmic Dawn Center (DAWN), Niels Bohr Institute, University of Copenhagen, Juliane Maries vej 30, DK-2100 Copenhagen, Denmark
[5] Department of Astronomy, University of Massachusetts, Amherst, MA 01003, USA
[6] Institute for Astronomy, Royal Observatory, University of Edinburgh, Edinburgh, EH9 3HJ, UK
[7] University of the Western Cape, Bellville, Cape Town 7535, South Africa
[8] South African Astronomical Observatory, Observatory, Cape Town 7925, South Africa
[9] Department of Physics and Astronomy and PITT PACC, University of Pittsburgh, Pittsburgh, PA 15260, USA
[10] Institute for Computational Science, University of Zurich, CH-8057 Zurich, Switzerland
[11] Department of Astronomy, University of California, Berkeley, CA 94720, USA
Received 2021 May 26; revised 2022 March 5; accepted 2022 March 11; published 2022 April 15

Abstract

Over the past decade, rest-frame color–color diagrams have become popular tools for selecting quiescent galaxies at high redshift, breaking the color degeneracy between quiescent and dust-reddened star-forming galaxies. In this work, we study one such color–color selection tool—the rest-frame $U-V$ versus $V-J$ diagram—by employing mock observations of cosmological galaxy formation simulations. In particular, we conduct numerical experiments assessing both trends in galaxy properties in *UVJ* space and the color–color evolution of massive galaxies as they quench at redshifts $z\sim1$–2. We find that our models broadly reproduce the observed *UVJ* diagram at $z=1$–2, including (for the first time in a cosmological simulation) reproducing the population of extremely dust-reddened galaxies in the top right of the *UVJ* diagram. However, our models primarily populate this region with low-mass galaxies and do not produce as clear a bimodality between star-forming and quiescent galaxies as is seen in observations. The former issue is due to an excess of dust in low-mass galaxies and relatively gray attenuation curves in high-mass galaxies, while the latter is due to the overpopulation of the green valley in SIMBA. When investigating the time evolution of galaxies on the *UVJ* diagram, we find that the quenching pathway on the *UVJ* diagram is independent of the quenching timescale, and instead dependent primarily on the average specific star formation rate in the 1 Gyr prior to the onset of quenching. Our results support the interpretation of different quenching pathways as corresponding to the divergent evolution of post-starburst and green valley galaxies.

Unified Astronomy Thesaurus concepts: Two-color diagrams (1724); Galaxy quenching (2040); Post-starburst galaxies (2176)

1. Introduction

Understanding and quantifying the rate of star formation at high redshift is key to constraining the formation of massive galaxies in the early universe. It has been widely observed that massive galaxies generally fall into two categories: blue, disk-dominated galaxies on the star-forming main sequence (SFMS), and red, elliptical, quiescent galaxies (Strateva et al. 2001; Baldry et al. 2004; Balogh et al. 2004; Bell et al. 2004; Faber et al. 2007). While quiescent galaxies are ubiquitous in the local universe, recent observations have detected massive quiescent galaxies out to $z\sim4$ (Glazebrook et al. 2017; Schreiber et al. 2018; Carnall et al. 2020; Forrest et al. 2020; Valentino et al. 2020). However, it can be difficult to identify quiescent galaxies and constrain their SFRs at high redshift owing to the ubiquity of dust-obscured star formation at $z\gtrsim1$, which can significantly redden star-forming galaxies (SFGs; Brammer et al. 2009; Maller et al. 2009).

Over the past decade, rest-frame color–color diagrams have become popular tools for breaking this degeneracy between SFGs reddened by dust and quiescent galaxies, intrinsically red due to older stellar populations. Such diagrams typically compare one color in the rest-frame near-UV (NUV) to optical range and another in the rest-frame optical–near-IR in order to cleanly separate quiescent and dusty SFGs (DSFGs) on the optical red sequence. While spectroscopic measures such as the Hα luminosity and $D_n(4000)$ index can serve as more reliable indicators of active star formation (e.g., Kauffmann et al. 2003), color–color diagrams can be readily applied to large surveys and at high redshift (e.g., Daddi et al. 2004; Labbé et al. 2005; Arnouts et al. 2007; Wuyts et al. 2007; Williams et al. 2009; Ilbert et al. 2013; Tomczak et al. 2014; Kriek et al. 2015; Fang et al. 2018; Wu et al. 2018; Carnall et al. 2019). In particular, the rest-frame $U-V$ versus $V-J$ (hereafter *UVJ*) diagram has proven an effective diagnostic for selecting quiescent galaxies across a range of redshifts (Wuyts et al. 2007; Williams et al. 2009; Whitaker & Labbé 2011; Muzzin et al. 2013; Fang et al. 2018). In addition to providing an accessible method for selecting quiescent galaxies, *UVJ* colors have been shown to correlate with specific star formation rates (sSFRs; Williams et al. 2010; Patel et al. 2011; Leja et al. 2019), dust attenuation (A_V; Price et al. 2014; Forrest et al. 2016; Martis et al. 2016; Fang et al. 2018), and stellar age (Whitaker et al. 2013; Belli et al. 2019; Carnall et al. 2019).

Despite its central role as a selection tool for high-redshift quiescent galaxies, much is still uncertain about the distribution of galaxy properties on the *UVJ* diagram. In particular, the inferred properties and interpretations of galaxy positions in *UVJ* space may be sensitive to the assumed dust attenuation curve. Often, at high redshift, all galaxies are assumed to follow a Calzetti et al. (2000) dust attenuation law, though recent evidence points to the likelihood that galaxies span a range of attenuation curves (Kriek & Conroy 2013; Scoville et al. 2015; Salmon et al. 2016; Leja et al. 2017; Narayanan et al. 2018; Salim et al. 2018; Salim & Narayanan 2020). While slopes and feature strengths of attenuation curves naturally correlate with galaxy properties such as SFR and M_* (Salim et al. 2018), much of the variation in attenuation curves seems to be driven by less constrained factors such as the complexity of the relative star−dust geometry (Seon & Draine 2016; Narayanan et al. 2018; Trayford et al. 2020). Indeed, the spread of galaxy colors in the star-forming region of *UVJ* space has been shown to be correlated with galaxy morphology and inclination (Patel et al. 2012; Zuckerman et al. 2021), and variations in the attenuation curve have been hypothesized to lead to *UVJ* misidentification (Roebuck et al. 2019). While the *UVJ* diagram has proven an effective tool, there is still a great deal of uncertainty regarding the utility of color–color diagrams in inferring galaxy properties, and independent measures of such properties are necessary to resolve this.

Furthermore, the ubiquity of the *UVJ* diagram as a selection and visualization tool at high redshift has sparked interest in how different galaxy evolutionary histories (i.e., different quenching mechanisms or timescales) manifest in *UVJ* space. For example, recently quenched post-starburst (PSB) galaxies have been observed to cluster in a unique region of *UVJ* space (Whitaker et al. 2012; Wild et al. 2016; Yano et al. 2016; Almaini et al. 2017; Suess et al. 2020). Similarly, Fang et al. (2018) identify a population of "transition" galaxies in the star-forming region of *UVJ* space but with suppressed SFRs and propose that the mass distribution of these transition galaxies implies a mass-dependent quenching path in *UVJ* space. Some authors have inferred the *UVJ* evolutionary tracks for galaxies based on their SFHs and modeling a relationship between SFR and dust attenuation (e.g., Barro & Faber 2014; Belli et al. 2019; Carnall et al. 2019; Suess et al. 2021). These model tracks support the view of an evolutionary pathway dependent on the quenching mechanism, in which faster-quenching PSB galaxies enter the quenched region from the bottom left and slower-quenching galaxies enter from the right (see e.g., Suess et al. 2021, Figure 12). However, these models are highly dependent on the assumed relationship between dust attenuation and SFR, which is unconstrained for galaxies at the epoch of quenching and may not be universal. A more complete and consistent theory for the evolution of galaxies in color–color space, though elusive, may provide efficient selection methods for studies of particular quenching processes.

In this light, cosmological simulations can help us understand and contextualize the distribution and evolution of galaxies on the *UVJ* diagram, as they provide easy access to fundamental galaxy properties over time. The *UVJ* selection technique has been explored in theoretical work in the past, and observations of the *UVJ* diagram have been broadly reproduced in cosmological (e.g., Davé et al. 2017; Donnari et al. 2019), zoom-in (e.g., Feldmann et al. 2017), and idealized (e.g., Roebuck et al. 2019) galaxy evolution simulations. As of yet, however, there has been no fully cosmological model that employs both realistic models of dust (to attend to the aforementioned issues of dust obscuration and attenuation) and radiative transfer (to model the mock colors) to thereby explore galaxies in *UVJ* space. The purpose of this paper is to develop and explore such a model.

In this work, we examine trends on the *UVJ* diagram using the SIMBA suite of simulations (Davé et al. 2019) and using the 3D dust radiative transfer code POWDERDAY (Narayanan et al. 2021). The structure of the paper is as follows. In Section 2 we describe the SIMBA simulations and the POWDERDAY dust radiative transfer code and outline our fiducial definitions. In Section 3 we compare our model *UVJ* diagram to observations with respect to both the distribution of *UVJ* colors (Section 3.1) and trends in galaxy properties in *UVJ* space (Section 3.2). This has the primary purpose of interrogating the simulations' ability to reproduce observations. In Section 4 we study the time evolution of galaxies in *UVJ* space with particular attention to the different pathways for quenching. We compare our models to those employed in other theoretical work in Section 5, and we summarize our conclusions in Section 6.

Throughout this paper, we adopt a Kroupa (2002) initial mass function (IMF) and a cosmology consistent with the Planck Collaboration (Planck Collaboration et al. 2016): $\Omega_m = 0.3$, $\Omega_\Lambda = 0.7$, $\Omega_b = 0.048$, $H_0 = 68\ \mathrm{km\ s^{-1}\ Mpc^{-1}}\ h^{-1}$, $\sigma_8 = 0.82$, and $n_s = 0.97$.

2. Methods

2.1. Simulations

This work utilizes the SIMBA simulations, a series of state-of-the-art cosmological hydrodynamic simulations of galaxy formation (Davé et al. 2019). The SIMBA simulations are the successor to the MUFASA (Davé et al. 2016) simulations and are run using a modified version of the gravity plus hydrodynamics solver GIZMO (Hopkins 2015), which uses the GADGET-3 tree-particle-mesh gravity solver (Springel 2005) and a meshless finite-mass method for hydrodynamics. A detailed description of the simulation physics and methodology has been presented in Davé et al. (2019). We refer the reader to this work for details and summarize the salient points here.

SIMBA models star formation using a molecular hydrogen (H_2) based Schmidt (1959) relation, where the H_2 fraction is computed using the subresolution model of Krumholz & Gnedin (2011) based on the metallicity and local column density, with minor modifications as described in Davé et al. (2016) to account for numerical resolution. The instantaneous SFR is thus given by the H_2 density divided by the dynamical time: $\mathrm{SFR} = \epsilon_* \rho_{\mathrm{H2}} / t_{\mathrm{dyn}}$, where we use $\epsilon_* = 0.02$ (Kennicutt 1998). Radiative cooling and photoionization heating are modeled using the GRACKLE-3.1 library (Smith et al. 2017), including metal cooling and nonequilibrium evolution of primordial elements. The chemical enrichment model tracks 11 metals during the simulation, with enrichment tracked from Type II supernovae (SNe), Type Ia SNe, and asymptotic giant branch (AGB) stars. Star-formation-driven galactic winds are modeled as decoupled two-phase winds, with 30% of wind particles ejected "hot," and with a mass loading factor that scales with stellar mass, based on the Feedback In Realistic Environments (FIRE; Hopkins et al. 2014) zoom simulation scalings from Anglés-Alcázar et al. (2017b).

SIMBA builds on MUFASA through the addition of black hole growth via torque-limited accretion (Hopkins & Quataert 2011; Anglés-Alcázar et al. 2013, 2015) and active galactic nucleus (AGN) feedback via bipolar kinetic outflows. Black holes are seeded and grown during the simulation, and the accretion energy drives feedback that acts to quench galaxies. For cold gas ($T < 10^5$ K), black hole growth is implemented following the torque-limited accretion model of Anglés-Alcázar et al. (2017a), which is based on Hopkins & Quataert (2011), while for hot gas ($T > 10^5$ K) Bondi accretion (Bondi 1952) is adopted. AGN feedback is implemented with a model designed to mimic the observed dichotomy of black hole growth and feedback modes observed (e.g., Heckman & Best 2014). In particular, real AGNs show a "radiative" mode at high Eddington ratios ($f_{\rm Edd}$) characterized by mass-loaded radiatively driven winds and a "jet" mode at low $f_{\rm Edd}$, characterized by high-velocity jets of $\sim 10^4$ km s^{-1}. The AGN outflow model has three modes of feedback: radiative, jet, and X-ray. Radiative and jet modes are implemented kinetically, with outflows ejected following a variable velocity and mass outflow rate to mimic the transition between high mass-loaded radiative winds and high-velocity jets. Full velocity jets are achieved at low Eddington ratios ($f_{\rm Edd} < 0.02$) and high black hole masses ($M_{\rm BH} > 10^{7.5}\,M_\odot$). X-ray feedback directly increases the temperature of gas not in the interstellar medium (ISM) and both heats and expels ISM gas. As shown in Davé et al. (2019), the jet mode is primarily responsible for quenching galaxies, while X-ray feedback has an important role in suppressing residual star formation.

Of particular relevance for this work, SIMBA includes a unique self-consistent on-the-fly subgrid model for the production, growth, and evolution of dust grains (described in detail in Davé et al. 2019; Li et al. 2019). Dust grains are assumed to have a single size of 0.1 μm and are passively advected with gas elements as a fraction of the element's metal budget. Dust grains grow via condensation following Dwek (1998) but with updated condensation efficiencies, as well as by accretion of gas-phase metals via two-body collisions. Dust is destroyed (returned back to the gaseous metal phase) by collisions with thermally excited gas following the analytic approximation of dust growth rates from Tsai & Mathews (1995). A mechanism for dust destruction via SN shocks is implemented following McKinnon et al. (2016). Dust is instantaneously destroyed in hot winds, during star formation, and in gas impacted by jet or X-ray AGN feedback; however, dust is not destroyed in cold star formation winds or radiative-mode AGN feedback to allow these winds to transport dust out of the galaxy. This model results in dust-to-metal ratios and dust mass functions in good agreement with observations for SFGs (Li et al. 2019).

The primary simulation we use in this work is the fiducial $(100\ {\rm Mpc}\ h^{-1})^3$ comoving volume, run from $z = 249$ to $z = 0$ with 1024^3 gas elements and 1024^3 dark matter particles. The minimum gravitational softening length is $\epsilon_{\rm min} = 0.5\ {\rm kpc}\ h^{-1}$, and the mass resolution is $9.6 \times 10^7\,M_\odot$ for dark matter particles and $1.8 \times 10^7\,M_\odot$ for gas elements. This simulation outputs 151 snapshots from $z = 20 \rightarrow 0$. We supplement our analysis with results from the high-resolution $(25\ {\rm Mpc}\ h^{-1})^3$ comoving box. This run includes 512^3 gas elements and 512^3 dark matter particles, with a mass resolution of $1.2 \times 10^7\ M_\odot$ and $2.3 \times 10^6\,M_\odot$ for dark matter and gas elements, respectively. In addition to 8 times higher mass resolution, the run outputs twice as many snapshots, for a total of 305 from $z = 20 \rightarrow 0$. This increased time resolution is the primary reason we include this simulation in this work; however, as a bonus, this provides a view of low-mass galaxies and serves as a test of numerical convergence. Unless otherwise stated, results are drawn from the $100\ {\rm Mpc}\ h^{-1}$ box.

Galaxy properties are computed and cataloged using CAESAR,[12] an extension of the YT simulation analysis software (Turk et al. 2011). CAESAR identifies galaxies using a 6D friends-of-friends algorithm with a spatial linking length of 0.0056 times the mean interparticle separation and a velocity linking length set to the local velocity dispersion. CAESAR outputs a cross-matched halo and galaxy catalog, from which the bulk of galaxy properties used in this work are drawn. Additionally, CAESAR includes a progenitor/descendant tracking module that identifies the major progenitor and descendant of a given galaxy at a given snapshot based on the number of star particles in common. We utilize this code to track galaxies across snapshots.

2.2. Fiducial Definitions

A consistent challenge for studies of the shutoff of star formation in galaxies is that there exists no standardized, widely accepted definition of "quenching." Here we present the SIMBA SFR–M_* relation, from which we establish our fiducial definition of quenching and compare to other common definitions.

Figure 1 shows the SFR–M_* relation for SIMBA at $z = 1$ and $z = 2$. Throughout this work, we compute SFRs by summing (and normalizing) the formation masses of star particles formed over the past 200 Myr.[13] Following Whitaker et al. (2014), we adopt a "bending" model for the SFMS and fit a second-order polynomial to the running median of log SFR in 0.2 dex bins of $\log M_*/M_\odot$. We perform this fit iteratively, each time limiting the next fit to only SFGs with SFRs within 0.5 dex of the main-sequence line computed in the previous iteration. We compute best-fit coefficients (labeled following Equation (2) of Whitaker et al. 2014) of $a = -25.02$, $b = 4.19$, and $c = -0.16$ at $z = 2$ and $a = -22.84$, $b = 3.95$, and $c = -0.16$ at $z = 1$. Figure 1 shows our MS fit alongside observational estimates for the SFMS from Speagle et al. (2014) and Whitaker et al. (2014). We find that our SFMS fit is in good agreement with observations, though notably it is lower in amplitude by $\sim$0.3 dex (as in Davé et al. 2019; Nelson et al. 2021).

We categorize galaxies based on their distance, in dex, from the SIMBA main sequence (ΔSFR). If $\Delta{\rm SFR} < -1$ dex, we define the galaxy as quenched; if $\Delta{\rm SFR} > -0.5$ dex, we consider it on (or above) the SFMS. These two dividing lines are shown as dashed–dotted and dashed lines in Figure 1, respectively. If ΔSFR is between these values, we consider the galaxy to be "transitioning" between the two populations. These fiducial definitions give a quenched fraction (for $M_* > 10^{10}\,M_\odot$) of 12% at $z = 2$ and 40% by $z = 1$. Of the "transitioning" population, $\sim$35% are rejuvenating (i.e., they have ${\rm SFR}_{50\ {\rm Myr}} > {\rm SFR}_{200\ {\rm Myr}}$) at both $z = 1$ and $z = 2$.

While we adopt this as our fiducial definition, the lack of a standardized definition of quenching makes it necessary to

[12] Available at https://github.com/dnarayanan/caesar.

[13] We use an averaging timescale of 200 Myr to balance the utility of instantaneous SFRs with the resolution of the simulations. For a thorough discussion, see Appendix A of Donnari et al. (2019).

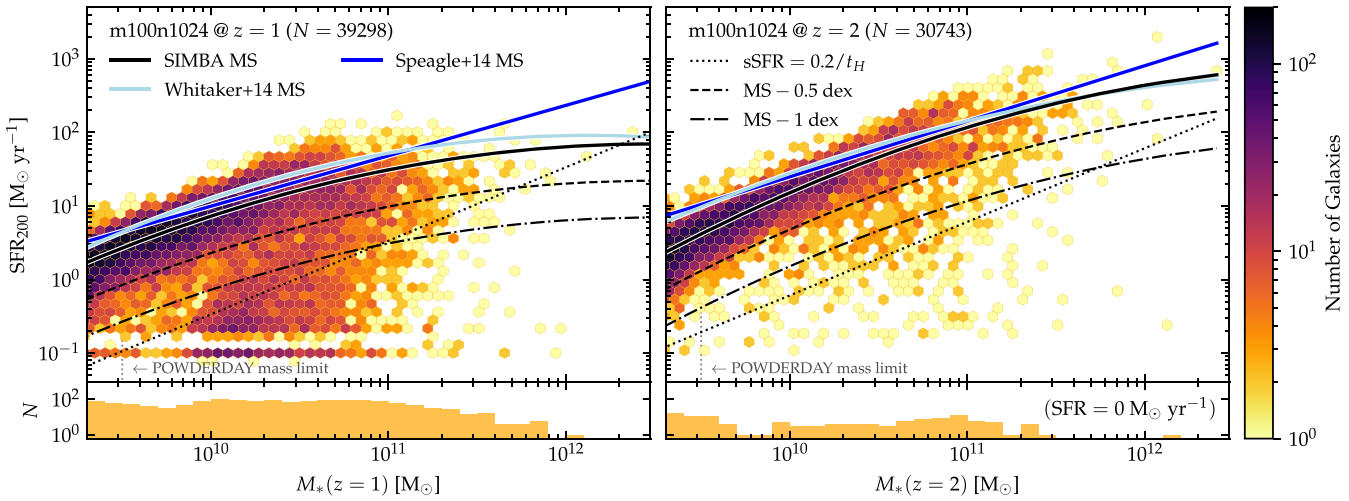

Figure 1. Hex bin plots of the SFR–stellar mass relation in our simulations at $z = 1$ (left panel) and $z = 2$ (right panel). The SFRs are averaged over the past 200 Myr, and the solid black line shows the best-fit second-degree polynomial for the SIMBA main sequence. The full sample of >30,000 resolved SIMBA galaxies is used to determine the main sequence. The dark- and light-blue lines show the MS relations from Speagle et al. (2014) and Whitaker et al. (2014), respectively. The dashed and dotted–dashed lines show the SIMBA MS $-$ 0.5 dex and MS $-$ 1 dex lines, respectively, which we use to separate between star-forming, transitioning, and quenched galaxies. A simple sSFR cut of sSFR $= 0.2/t_{\rm H}$, where $t_{\rm H}$ is the Hubble time at that redshift, is also shown as a dotted line. The histogram in the lower panel shows the distribution of galaxies with no resolved star formation in the past 200 Myr, and the distinct horizontal feature at SFR $\sim 10^{-1}\ M_\odot\ {\rm yr}^{-1}$ corresponds to the smallest resolvable SFR.

compare this choice to others. Figure 1 also shows a time-evolving cut in the sSFR ($=$ SFR$/M_*$) commonly used to define quenching (e.g., Pacifici et al. 2016; Rodríguez Montero et al. 2019). Additionally, though not shown, we explore a cut in the normalized SFR (nSFR), the ratio of a galaxy's current SFR to its lifetime average SFR. We find that the nSFR $= 0.1$ cut adopted by Carnall et al. (2018) is in good agreement with the sSFR cut shown in Figure 1, and both of these definitions broadly agree with our MS $-$ 1 dex cut. Though our ΔSFR definition of quenching is more lenient (i.e., includes more quenched galaxies) at low masses and more strict at higher masses, our results are not sensitive to this definition.

2.3. 3D Dust Radiative Transfer

To extract observables from the simulation, we use the 3D dust radiative transfer code POWDERDAY.[14] POWDERDAY provides a convenient, modular, and parallelizable framework for computing the dust-attenuated spectral energy distributions (SEDs) of galaxies in cosmological simulations. Fundamentally, the code weaves together FSPS (Conroy & Gunn 2010; Conroy et al. 2010) for stellar population synthesis (SPS), HYPERION (Robitaille 2011) for Monte Carlo radiative transfer, and YT (Turk et al. 2011) for interfacing with cosmological simulation data. POWDERDAY is described in detail in Narayanan et al. (2021); here we summarize the relevant points.

For each galaxy identified by CAESAR, we perform SPS using FSPS (Conroy & Gunn 2010; Conroy et al. 2010). We treat each star particle as a simple stellar population (SSP) with a fixed age and metallicity taken directly from the simulation. These properties are then provided to FSPS, which generates a stellar SED assuming an IMF combined with theoretical isochrones. We adopt MIST isochrones (Choi et al. 2016; Dotter 2016; Paxton et al. 2011) and a MILES stellar spectra library (Sánchez-Blázquez et al. 2006) as our fiducial choice of SPS parameters. We explore in Section 3.1.1 the impact of the assumed isochrones on the resulting *UVJ* diagram. Stellar SEDs for three example galaxies are shown as blue lines in the bottom right panels of Figure 2.

We then compute the attenuated SEDs by performing dust radiative transfer. The dust properties stored in the gas elements in the simulation are projected on an adaptive octree grid. We then allow radiation from sources to propagate through the dusty ISM of the galaxy, which acts to scatter, absorb, and reemit incident radiation. This is done in a Monte Carlo fashion in HYPERION (Robitaille 2011). Photon packets are released with random direction and frequency and propagate until they escape the grid or reach some limiting optical depth, and an iterative procedure is used to calculate the equilibrium dust temperature. The output SEDs are then calculated through ray-tracing; such SEDs are shown as red lines in Figure 2. In this work, the viewing angle for ray-tracing is fixed relative to the coordinate system of the cosmological box. Though the viewing angle is a flexible parameter, fixing it this way means that the observed inclination of a given galaxy is effectively random, as in observations.

While we adopt POWDERDAY as our fiducial method for modeling dust attenuation, we compare the resulting *UVJ* diagrams to those derived from other modeling approaches in Section 3.1.2. We note that the combination of the SIMBA explicit dust model and POWDERDAY radiative transfer has had great success in reproducing observations of dusty galaxies, including matching the observed number density of high-redshift submillimeter galaxies (Lovell et al. 2021), as well as the observed dust-to-gas and dust-to-metals ratios at low and high redshift (Li et al. 2019).

2.4. Sample Selection and Photometry

Though we use the full sample of resolved SIMBA galaxies to define the MS, it would be computationally intractable to run radiative transfer on this full sample. Instead, we select galaxies with $\log M_*/M_\odot > 9.5$ from the $(100\,h^{-1}\,{\rm Mpc})^3$ simulation, which corresponds to ~250 star particles and ~500 gas elements. In this work, we focus primarily on the SIMBA

[14] Available at https://github.com/dnarayanan/powderday.

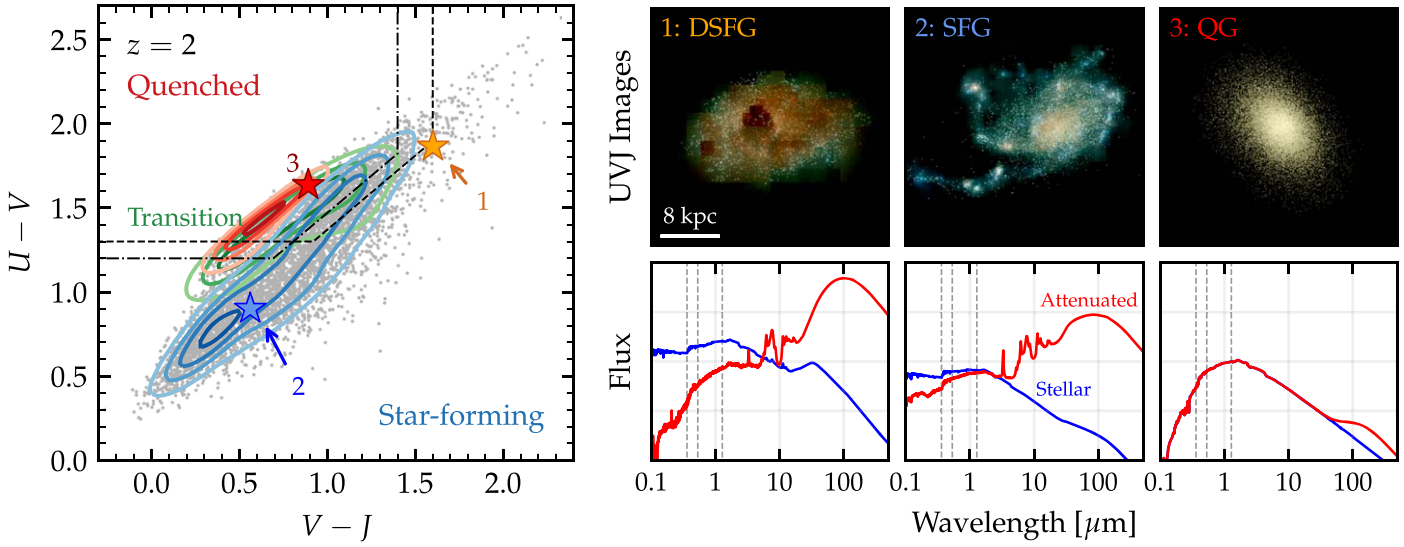

Figure 2. Overview of the *UVJ* diagram derived from POWDERDAY radiative transfer. Left: the SIMBA *UVJ* diagram at $z = 2$. KDE contours for the quenched galaxies, transitioning galaxies, and SFGs are plotted in shades of red, green, and blue, respectively, and our galaxy sample is plotted in the background. The dashed and dashed–dotted lines show the $z = 2$ *UVJ* selection criteria of Williams et al. (2009) and Whitaker & Labbé (2011), respectively. Stars indicate the *UVJ* colors of three example galaxies: (1) a DSFG, (2) a nondusty SFG, and (3) a quenched galaxy (QG). Top right: simulated *UVJ* images of these three example galaxies derived from POWDERDAY. Particularly star-forming and particularly dusty regions can be seen in blue (*U* band) and red (*J* band), respectively. Bottom right: stellar and dust-attenuated SEDs for these three example galaxies. The central wavelengths of the *U*, *V*, and *J* bands are indicated as dashed lines behind the SEDs.

snapshots at $z = 2$ and $z = 1$, as these span the range of redshifts at which *UVJ* selection is most often used. At $z = 2$ our mass-limited sample contains 5795 galaxies, while at $z = 1$ it contains 12,035 galaxies.

We compute the rest-frame *U*, *V*, and *J* magnitudes by convolving the SED generated by POWDERDAY with the corresponding filter transmission curve. Specifically, we use the Bessell (1990) *U* and *V* curves and the Maunakea UKIRT WFCAM curve for *J* (Hewett et al. 2006). While we do not apply any apertures to these photometric measurements, we have verified that the resulting *UVJ* diagram is largely unchanged by the use of 0.″7 radius apertures as in the 3D-HST survey (Skelton et al. 2014). Additionally, we show in Appendix B the model *UVJ* diagram with the addition of mock observational noise, specifically the noise resulting from ∼5% uncertainty in the photometric redshift. This noise scatters galaxies in all directions, producing a *UVJ* diagram that, qualitatively, more closely resembles observations. However, as this noise may obscure the trends of interest in our work, we do not include this in our fiducial model.

3. Observational Comparisons

Before exploring the evolution of simulated galaxies in *UVJ* space, we perform comparisons to observations to determine whether our simulations and radiative transfer methodology can adequately reproduce observations, and where they cannot, we diagnose the underlying issues.

First, we present in Figure 2 our fiducial *UVJ* diagram at $z = 2$. Here we denote the distribution of star-forming, transitioning, and quenched galaxies via contours. The right panels show SEDs and simulated *UVJ* images for three example galaxies drawn from the simulation box: a DSFG, a nondusty SFG, and a quenched galaxy. We broadly reproduce the observed distribution of *UVJ* colors, in that we see distinct clustering of quiescent galaxies along the top left, a star-forming sequence along the bottom right, and transition galaxies in between.

However, our models are in tension with observations in two notable ways. First, we do not produce as clear of a bimodal distribution of galaxies as is observed, that is, we see more overlap between the quiescent and star-forming populations. Second, our colors are generally bluer than observations, with a significant number of DSFGs populating the quiescent region as defined by Williams et al. (2009) and Whitaker & Labbé (2011). We explore these discrepancies further in the following subsections, first by focusing only on the distribution of *UVJ* colors and then by examining trends in galaxy properties on the *UVJ* diagram.

3.1. Distribution of UVJ Colors

3.1.1. Dependence on Stellar Population Models

First, we examine how well SIMBA matches the observed distribution of rest-frame *UVJ* colors within the context of the underlying stellar model. We do so by comparing the SIMBA +POWDERDAY *UVJ* diagram, under different model assumptions, to the observed sample from the 3D-HST survey at $1.7 < z < 2.3$ (Brammer et al. 2012; Skelton et al. 2014; Momcheva & Brammer 2016).

Figure 3 shows the SIMBA *UVJ* diagram at $z = 2$ for three different SPS models. Specifically, we show the *UVJ* diagram for three different assumed stellar isochrones: MIST, which includes rotating stars (Paxton et al. 2011; Choi et al. 2016; Dotter 2016); BPASS, which includes binary stars (Eldridge et al. 2017); and Padova (Bertelli et al. 1994; Girardi et al. 2000; Marigo et al. 2008). While red, green, and blue contours show the distributions for quenched galaxies, transition galaxies, and SFGs in SIMBA, respectively, the gray contours show the 3D-HST sample. For each of the star-forming, transition, and quiescent populations, we plot the outliers as colored points. In each panel, we show histograms of $U - V$ and $V - J$ colors for each isochrone.

Immediately, it is apparent that there is some disagreement between the SIMBA *UVJ* diagram and the 3D-HST data.

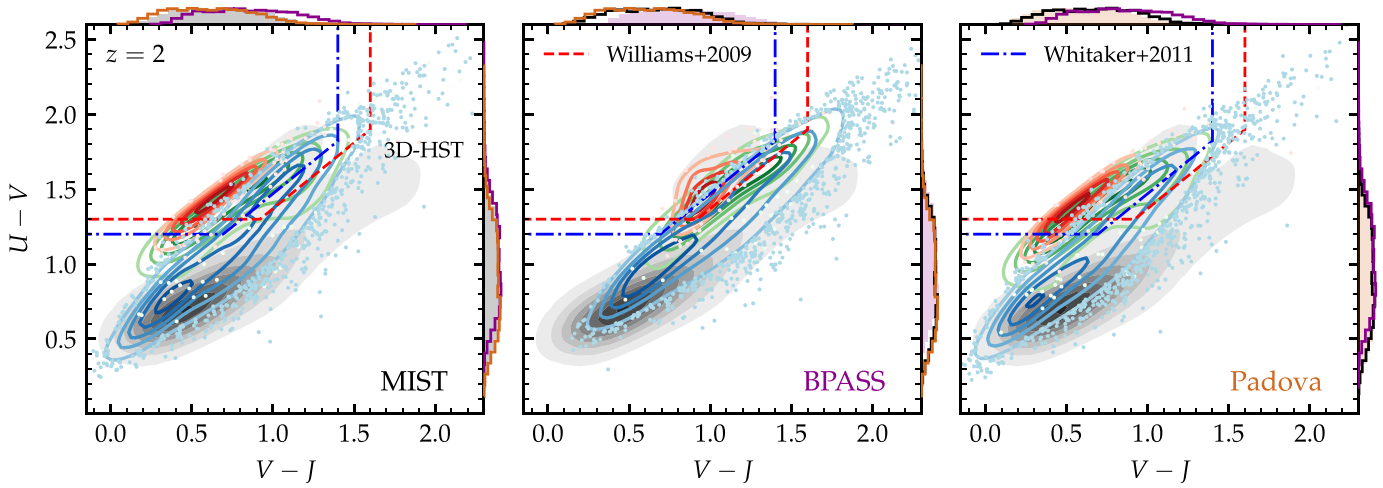

Figure 3. Comparison of mock *UVJ* colors to 3D-HST observations. The plot additionally shows the impact of different stellar isochrones on the model *UVJ* diagram in SIMBA. Contours and observational *UVJ* selection criteria from Williams et al. (2009) and Whitaker & Labbé (2011) are shown as in Figure 2. We additionally show the outliers for each population as colored points. From left to right, the panels show *UVJ* diagrams computed from POWDERDAY using MIST, BPASS, and Padova isochrones. Histograms on the axes show the distributions of $U - V$ and $V - J$ colors for each stellar isochrone choice, with the one particular to that panel filled in and the others as outlines.

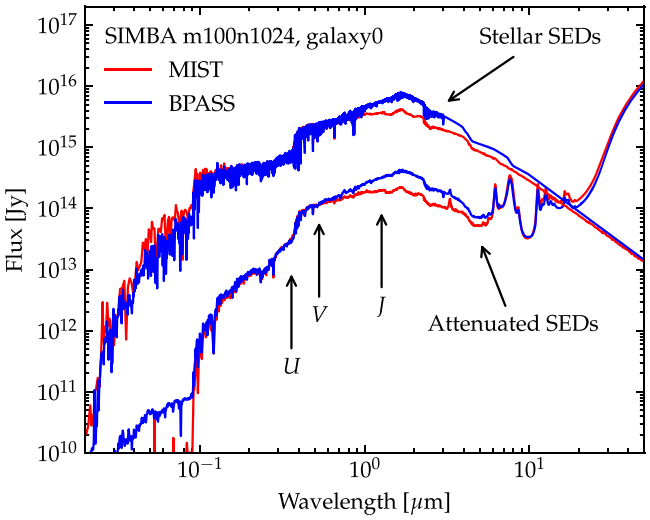

Figure 4. SEDs for an example galaxy from our simulations at $z = 2$ using both MIST (red) and BPASS (blue) isochrones. Stellar and attenuated SEDs are shown, and we see that BPASS produces systematically redder colors owing to a bump in the SED in the J band.

Specifically, while we predict a similar range of colors, we generally have bluer colors than the observational data. This is true for MIST and Padova isochrones; however, BPASS isochrones produce generally redder colors, more in line with the 3D-HST sample. Figure 4 shows (stellar and dust-attenuated) SEDs for an example galaxy computed with MIST and BPASS isochrones. We see that the systematically redder colors we get from BPASS isochrones are primarily due to a bump in the SED near the J band.

While the systematically redder colors produced from BPASS isochrones bring our results in closer agreement with observational selection criteria, they also noticeably change the distribution of galaxies on the *UVJ* diagram. The overlap between the quenched and star-forming populations is more significant in the BPASS model, with only a handful of quenched galaxies extending beyond the region occupied by SFGs. Additionally, BPASS places the oldest, reddest quiescent galaxies at the same $V - J$ as their younger counterparts, in contrast to observations (e.g., Whitaker et al. 2013). As such, we adopt MIST isochrones in our fiducial SPS model, with the caveat that our colors are generally bluer than observations. However, we interpret this as a systematic effect and move forward with the assumption that our fiducial models broadly reproduce the observed *UVJ* diagram modulo this $\sim$0.2–0.3 mag shift. The significant contamination of the quiescent region from SFGs in our model is primarily due to this systematic color shift.

3.1.2. Dependence on Dust Models

We next turn to understanding how the comparison between our model galaxies and those observed in *UVJ* space depends on the assumed underlying dust model.

Figure 5 shows the SIMBA *UVJ* diagram at $z = 2$ using three different dust models: the explicit dust model in SIMBA, in which gas particles keep track of dust creation, growth, and destruction on the fly in the cosmological simulation; a dust-to-metals model, in which dust mass is assumed to scale with the metal mass by a constant ratio of 0.4; and a simplified line-of-sight (LOS) extinction model, in which galaxies are assumed to follow an sSFR and metallicity-dependent extinction law. The former two models employ POWDERDAY radiative transfer in which dust is distributed throughout the galaxy as computed in the hydrodynamic galaxy formation simulations, whereas the latter model simply sums the LOS extinction from each star particle. This model is included primarily to demonstrate the importance of radiative transfer in computing realistic colors (e.g., Narayanan et al. 2021).

It is clear from Figure 5 that only the combination of the SIMBA explicit dust model and POWDERDAY radiative transfer is able to fully populate the dusty star-forming region of *UVJ* space (the top right of the diagram). These incredibly red, dusty galaxies have historically been a challenge for simulations to reproduce (e.g., Davé et al. 2017; Donnari et al. 2019), and even proved challenging for early observational surveys (e.g., Williams et al. 2009) owing to a lack of sufficiently red template SEDs in rest-frame color measurements (see

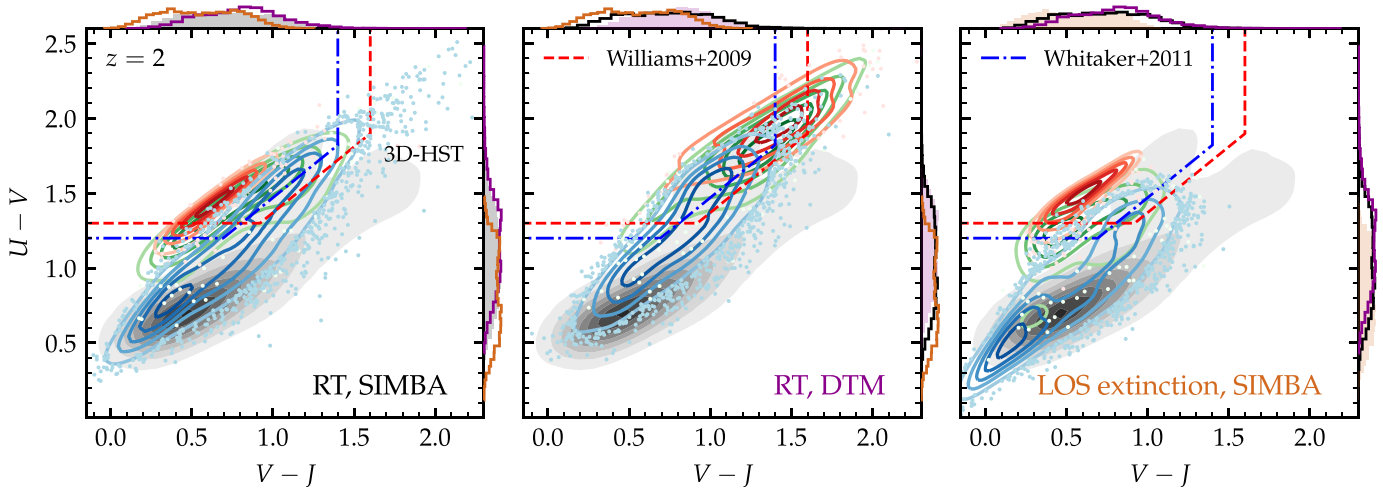

Figure 5. Impacts of different dust models on the *UVJ* diagram in SIMBA. Contours and points are shown as in Figure 3. From left to right, the panels show *UVJ* diagrams using POWDERDAY with the SIMBA explicit dust model, using POWDERDAY with a dust-to-metals ratio of 0.4, and using an LOS extinction model with an sSFR and metallicity-dependent extinction law. Histograms on the axes show the distributions of $U - V$ and $V - J$ colors for each dust model choice, with the one of that panel filled in and others as outlines.

Appendix C in Whitaker et al. 2010). As such, the success of our SIMBA+POWDERDAY dust model serves as an indicator of the critical importance of modeling dust physics explicitly when simulating broadband *UVJ* colors. For example, the dust-to-metals model produces redder colors for quiescent galaxies than for dust SFGs, as these quiescent objects are some of the most metal-enriched objects in the simulation. This is inconsistent with the observed colors of galaxies at $z \sim 2$. At the same time, the LOS extinction model, even incorporating the SIMBA explicit dust masses, fails to properly populate the top right of the diagram.

Additionally, though not shown, we examine the effects of varying other model assumptions. We find little ($\sim$0.03 mag) difference in *UVJ* colors resulting from varying the stellar IMF between those of Kroupa (2002), Chabrier (2003), and Salpeter (1955). We find a comparably small difference in *UVJ* colors from varying the spectral library from the MILES (Sánchez-Blázquez et al. 2006) and BaSeL (Westera et al. 2002) libraries. We find nearly no variation in *UVJ* colors from the inclusion of attenuation by circumstellar AGB dust (using the model of Villaume et al. 2015), AGN emission and dust model using SED templates from Nenkova et al. (2008a, 2008b), or nebular line and continuum emission from CLOUDY lookup tables (Byler et al. 2017, 2018, 2019; Narayanan et al. 2021; Garg et al. 2022).

3.2. Galaxy Physical Properties in UVJ Space

We have demonstrated that SIMBA+POWDERDAY can broadly reproduce the observed distribution of *UVJ* colors, with a few notable exceptions: we do not reproduce the clear bimodal number density in *UVJ* space, and we produce systematically bluer colors than observations. To further interrogate these inconsistencies with observations, we investigate the distribution of galaxy properties on the *UVJ* diagram and compare, qualitatively, to observed trends.

3.2.1. Dust Attenuation

We begin with an examination of trends in the dust attenuation A_V in our model *UVJ* diagram at $z = 1 - 2$. In Figure 6, we show our mock *UVJ* colors for our model galaxies at $z = 1$ and $z = 2$ for both a model without dust (i.e., discarding all of the dust content in our radiative transfer models) and a model including our fiducial dust model. Generally, without dust, galaxies form a relatively tight locus with a clear trend in ΔSFR. This is in line with dust-corrected *UVJ* diagrams inferred from observations (e.g., Fang et al. 2018). Including dust decreases the fidelity of this trend significantly as dust reddening pushes SFGs toward redder $V - J$ colors. We note that there are a small number of quiescent galaxies at $z = 1$ with dust-free colors placing them outside the quiescent region. This is due to a recent frosting of star formation, which we explore further in Section 3.2.3.

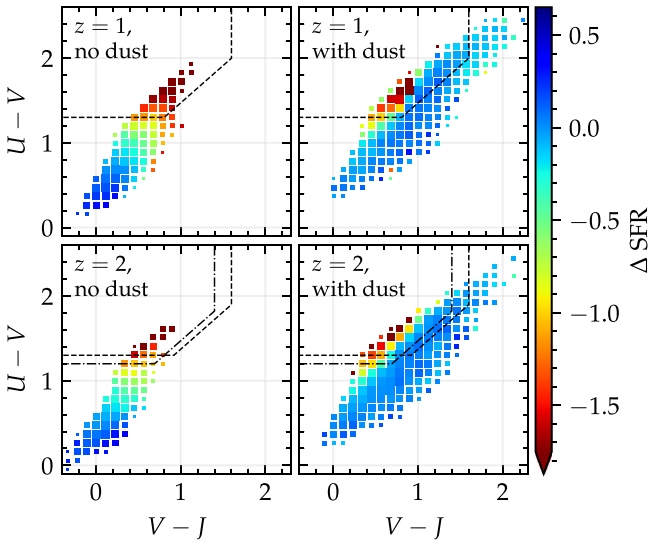

Figure 6. The SIMBA *UVJ* diagram at $z = 1$ (top) and $z = 2$ (bottom), both including the effects of dust (right column) and ignoring all dust (left column). We show the median ΔSFR in bins of $U - V$ and $V - J$, with points sized logarithmically according to the number of galaxies in the bin. While our dust-free models produce a clear gradient in ΔSFR according to $U - V$ color, including the effects of dust in our radiative transfer models moves SFGs to redder colors.

In Figure 7, we show our galaxies in *UVJ* space, color-coded by A_V. We first highlight the right column, which shows the

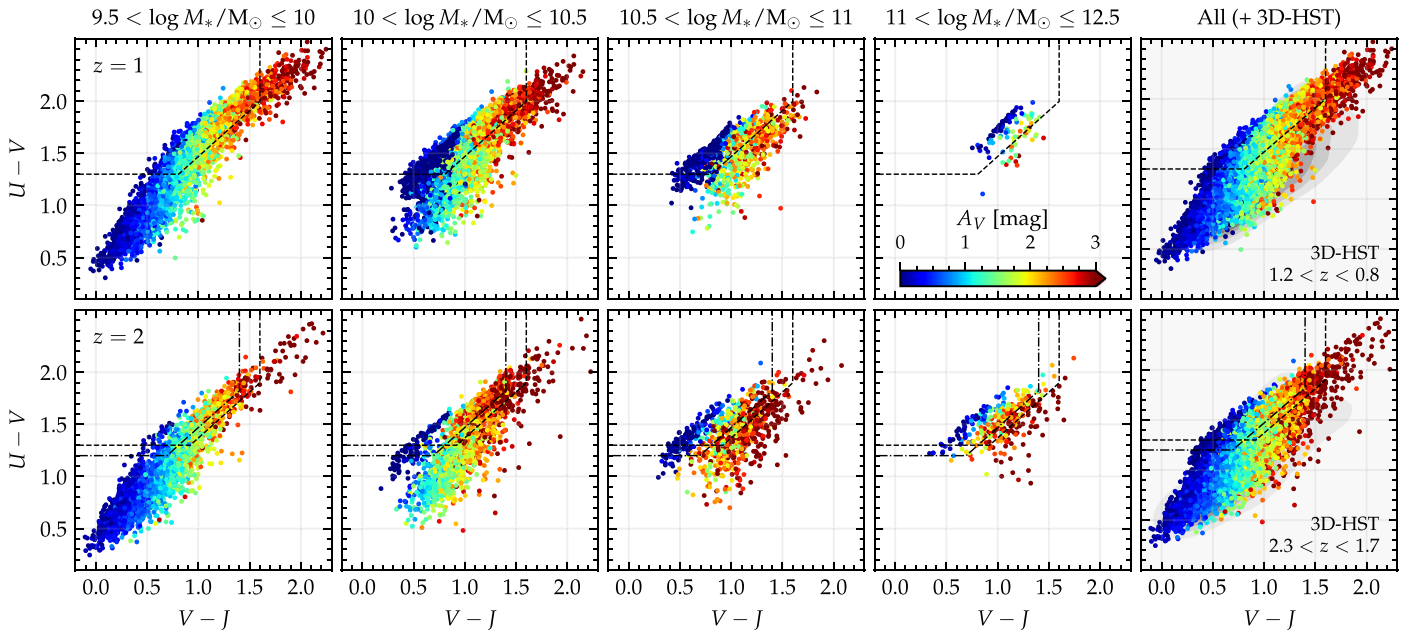

Figure 7. The SIMBA *UVJ* diagram in 4 bins of stellar mass. The top (bottom) row shows data for $z = 1$ ($z = 2$), and points are colored by the *V*-band dust attenuation A_V. The right column shows all model galaxies overplotted with KDE contours showing observations from the 3D-HST survey (Brammer et al. 2012; Momcheva & Brammer 2016). A strong correlation between A_V and $V - J$ color is evident at low masses but breaks down at higher masses, where many heavily attenuated galaxies have low $V - J$.

entire model galaxy sample for $z \sim 1$ (top) and $z \sim 2$ (bottom), with contours showing observations from the 3D-HST survey (Brammer et al. 2012; Skelton et al. 2014; Momcheva & Brammer 2016). Consistent with observational constraints (e.g., Price et al. 2014; Martis et al. 2016; Fang et al. 2018), we see lines of constant A_V for SFGs at roughly constant $V - J$. That said, this is a nuanced and mass-dependent trend. While we see a strong correlation between A_V and $V - J$ color for SFGs in the $9.5 < \log M_*/M_\odot \leqslant 10$ mass bin, at $10 < \log M_*/M_\odot \leqslant 10.5$ several highly dusty ($A_V \gtrsim 2.5$) galaxies show bluer $V - J$ colors than expected, and this trend continues to weaken at higher masses. Observational surveys (e.g., Fang et al. 2018) tend to find high-mass ($\log M_*/M_\odot > 10$) galaxies in the DSFG region on the far top right of the *UVJ* diagram and low-mass ($\log M_*/M_\odot < 10$) galaxies concentrated in the bottom left. The population of low-mass, highly dust-reddened galaxies in SIMBA is likely a by-product of our dust evolution model (Li et al. 2019), as observations typically do not find galaxies at this mass with $A_V \gtrsim 1$. Thus, while we successfully populate the dusty star-forming region of the *UVJ* diagram, we do so primarily with low-mass ($\log M_*/M_\odot \lesssim 10.5$) galaxies, rather than higher-mass galaxies as is seen in observational surveys. This, alongside the lack of a clear bimodality in our *UVJ* diagram, represents notable tensions with observations.

To further explore the relationship between mass, A_V, and attenuation curve slope (which impacts galaxy location in *UVJ* space), we show in Figure 8 the amount of dust reddening (defined as $A_V - A_J$) as a function of A_V for SFGs in SIMBA at $z = 2$. $A_V - A_J$ effectively measures the slope of the attenuation curve between the *V* and *J* bands, and galaxies with higher $A_V - A_J$ will be found farther to the right in *UVJ* space. We bin the sample into four bins of stellar mass and plot the median $A_V - A_J$ in each bin. We additionally plot the relationship of $A_V - A_J$ versus A_V for the literature attenuation curves of Cardelli et al. (1989) and Calzetti et al. (2000). We see that at $A_V \gtrsim 1$ our model galaxies generally show grayer attenuation curves than is expected for galaxies at this redshift. Moreover, at the same A_V, higher-mass galaxies in SIMBA experience less dust reddening, i.e., they have grayer attenuation curves. That is, as our simulated galaxies become more massive, the star −dust geometry becomes increasingly complex, and the attenuation curves become flatter (grayer) as stars and dust are spatially decoupled. This results in less pronounced reddening for the most massive galaxies.

As a check, we also show in the right panel of Figure 8 a scatter plot of the dust masses versus the stellar masses of the same sample of $z = 2$ SFGs.[15] We see that our high-mass galaxies still retain significant dust masses. This is consistent with recent observational constraints by Shapley et al. (2020) and Dudzevičiūtė et al. (2021), which have found that the SIMBA dust model reasonably reproduces the dust-to-gas ratio and dust mass function at $z \sim 2$. Similarly, the recent review by Péroux & Howk (2020) shows that the SIMBA model accurately reproduces observational constraints on the evolution of the cosmic dust density. This suggests that the absolute dust contents in our model galaxies are reasonable and reaffirms that the lack of high-mass, highly reddened galaxies must be due to the lack of obscuration and relatively gray attenuation laws.

Therefore, one possibility for reducing tensions with observations would be if our galaxies had steeper attenuation laws. Indeed, some observations have inferred laws steeper than those presented in our models in Figure 8 (e.g., McLure et al. 2018). While a quantitative comparison between the attenuation curves for SFGs in our model and those observed is outside the scope of this paper (though see Salim & Narayanan 2020), we note that the observational derivation of dust attenuation curves from unresolved systems at high *z* comes with significant attendant uncertainties, including

[15] While we show these trends only for $z = 2$ SFGs, we have confirmed that they hold at $z = 1$. We show these trends only for SFGs, as quiescent galaxies in SIMBA almost universally have $A_V \sim 0$.

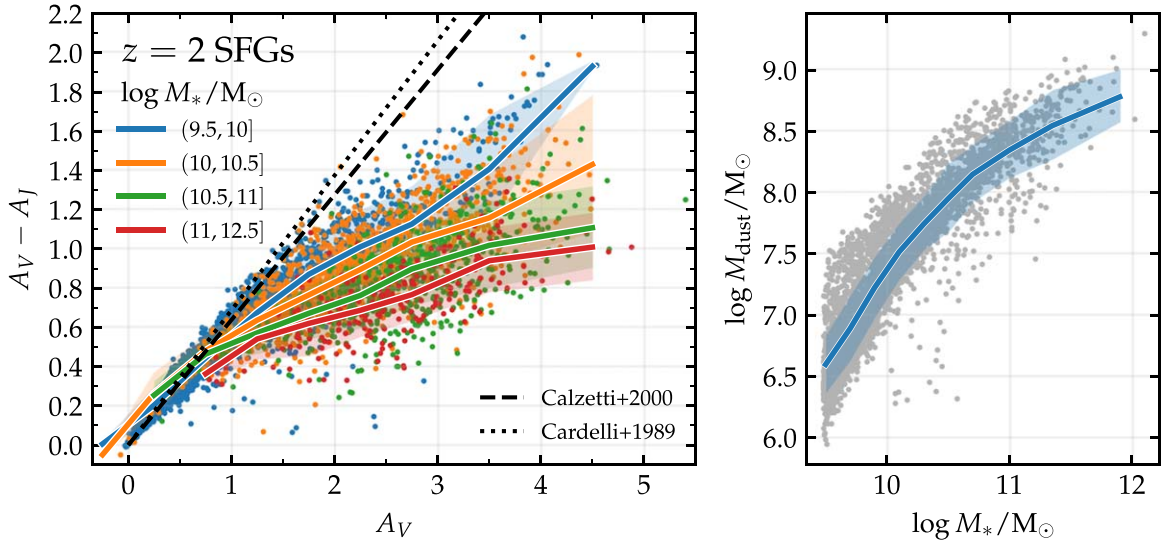

Figure 8. Left: relationship between dust reddening ($A_V - A_J$) and A_V for SFGs at $z = 2$. We bin the sample into four bins of stellar mass (as in Figure 7) and plot (for each mass range) the median $A_V - A_J$ in 10 bins of A_V. We see that, at the same A_V, higher-mass galaxies experience less dust reddening. Right: scatter plot of dust mass vs. stellar mass for the same sample of SFGs at $z = 2$, with KDE contours overlaid. We see that our high-mass galaxies still retain high dust masses, suggesting that the lack of high-mass galaxies in the dusty star-forming region of *UVJ* space is driven by grayer attenuation curves rather than a lack of dust content.

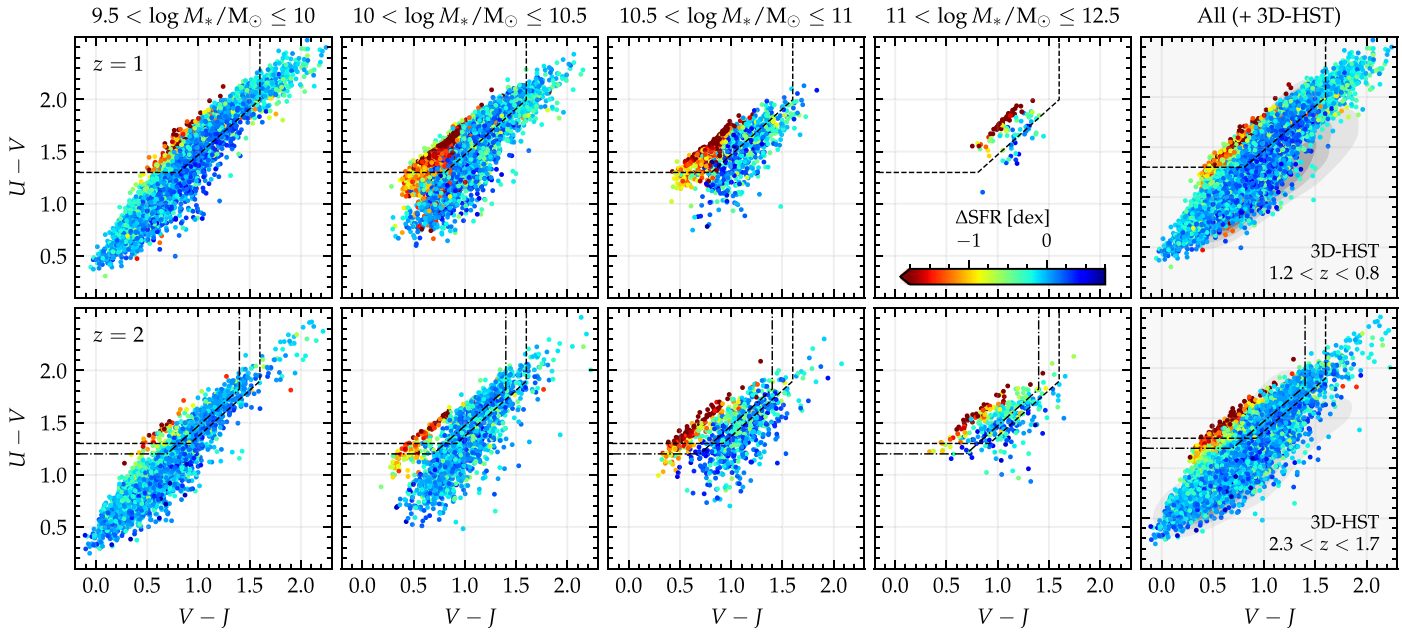

Figure 9. Same as Figure 7, but with points colored by the distance from the SFMS, ΔSFR. We see that star-forming and quiescent galaxies are well separated by the *UVJ* selection line and a mass trend is evident in the star-forming population.

assumed SED shapes (and location in IRX$-\beta$ space), as well as the shape of the intrinsic stellar continuum (Narayanan et al. 2018b; Reddy et al. 2018). Therefore, we move on with the assumption that our dust model reasonably reproduces the observed *UVJ* diagram, though it fails to produce adequate dust reddening in the highest-mass galaxies.

3.2.2. Star Formation Rates

We now examine trends with galaxy SFRs in *UVJ* space. In Figure 9, we show the $z = 1$ and $z = 2$ *UVJ* diagrams in 4 bins of stellar mass. Points are colored by each galaxy's distance, in dex, from the SFMS (ΔSFR). Despite the lack of a clear bimodality, quiescent galaxies and SFGs are well separated in *UVJ* space at all mass ranges, with quiescent galaxies occupying a narrow locus on the top left and SFGs populating the blue cloud. In between these two populations lie transition galaxies.

Numerous observational studies have found "stripes" of constant sSFR running roughly parallel to the diagonal selection line in *UVJ* space, with the youngest, most actively SFGs along the bottom right (Williams et al. 2009, 2010; Patel et al. 2011; Whitaker et al. 2012; Fang et al. 2018; Leja et al. 2019). This trend has generally been interpreted as support for the efficacy of *UVJ* selection of quiescent galaxies. This sSFR trend is somewhat subtle in our simulations and, at face value, appears at odds with observational constraints. We posit that tension is simply a manifestation of the diverse nature of dust attenuation curves in high-z galaxies. When deriving properties

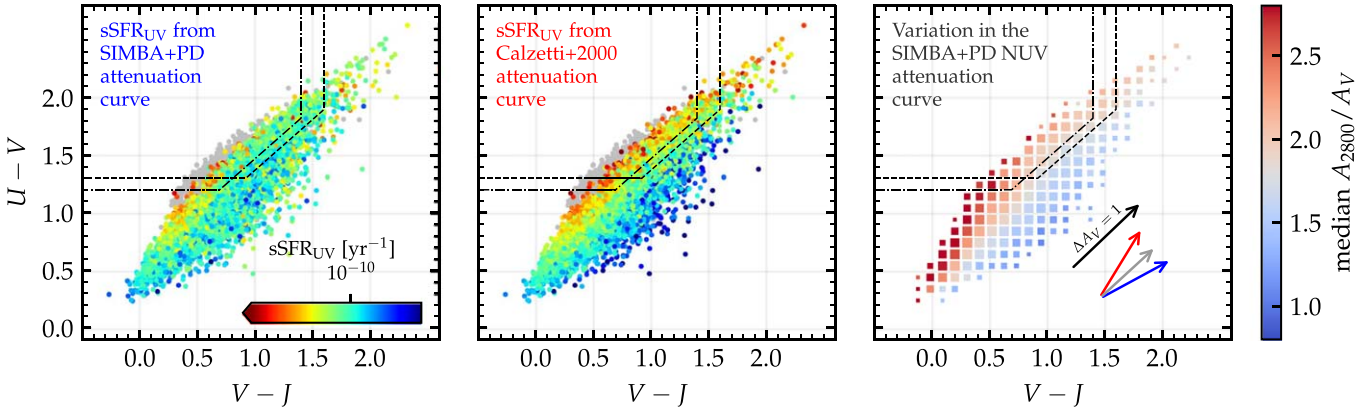

Figure 10. SFGs on the *UVJ* diagram at $z = 2$, with points colored by dust-corrected UV-derived sSFRs. In the left panel, dust correction is done using the true SIMBA +POWDERDAY attenuation curve. In the middle panel, dust correction is done assuming a universal Calzetti et al. (2000) attenuation curve as described in the text. The right panel shows the median ratio of the NUV attenuation A_{2800} to A_V, in bins of $U - V$ and $V - J$. The color bar is centered on $A_{2800}/A_V = 1.8$, the value for the Calzetti curve. Points are sized logarithmically according to the number of galaxies in that bin. Arrows show the "dust vector," or the effect on the *UVJ* colors of adding $\Delta A_V = 1$, for the Calzetti curve (black), as well as the median and the 25th and 75th percentile SIMBA curves (red, gray, and blue). Due in large part to varying dust vectors, the optical−NUV slope of the attenuation curve is correlated with the *UVJ* colors of SFGs. As such, the assumption of a universal attenuation curve exaggerates the subtle trend in sSFR on the *UVJ* diagram.

from SEDs at high redshift, many observations assume a universal Calzetti et al. (2000) dust attenuation law; in contrast, our simulations (as do many; e.g., Narayanan et al. 2018; Lagos et al. 2020; Trayford et al. 2020) yield wildly varying attenuation curves for high-z galaxies. This mismatch in assumed versus actual attenuation curve can bias properties derived from dust-corrected SEDs.

To examine this, we calculate dust-corrected UV SFRs following Fang et al. (2018) as

$$\mathrm{SFR_{UV}}\,[M_\odot\ \mathrm{yr}^{-1}] = 2.59 \times 10^{-10}\, L_{2800}\, 10^{0.4\,A_{2800}}, \qquad (1)$$

where L_{2800} is the 2800 Å luminosity from the SED (in $L_\odot$) and A_{2800} is the corresponding attenuation (in mag). We perform these calculations in two ways: first by using the actual A_{2800} values from POWDERDAY (i.e., employing the true dust attenuation curve for our model galaxies), and second by using the assumption of a Calzetti et al. (2000) law where $A_{2800} = 1.8A_V$. Figure 10 shows how these different attenuation curve assumptions produce different estimates of the sSFR. We show SFGs at $z = 2$, with points colored by sSFR$_{UV}$ computed assuming POWDERDAY attenuation curves (left panel) and assuming a Calzetti curve (middle panel).

Different attenuation curve assumptions—either a universal or widely varying attenuation curve—can impact trends in sSFR in *UVJ* space. To illustrate this, we show in the right panel of Figure 10 the relationship between galaxy positions in *UVJ* space and the optical−NUV slope of the SIMBA +POWDERDAY attenuation curve. The color map in this panel is centered on $A_{2800}/A_V = 1.8$, the value for a Calzetti law. We see that, for SFGs, the shape of the attenuation curve is correlated with the galaxy's location on the *UVJ* diagram. In particular, galaxies near the quenched region have a steeper attenuation curve in the $U - V$ and therefore have a steeper "dust vector" (the arrows shown in Figure 10). For galaxies on the bottom right, the opposite is true. This implies that if the true attenuation curves indeed vary, the assumption of a universal Calzetti law would tend to underestimate SFRs near the quenched region and overestimate along the bottom right.

There is evidence in the literature that the spread of SFGs in *UVJ* space is driven by structural properties and observed

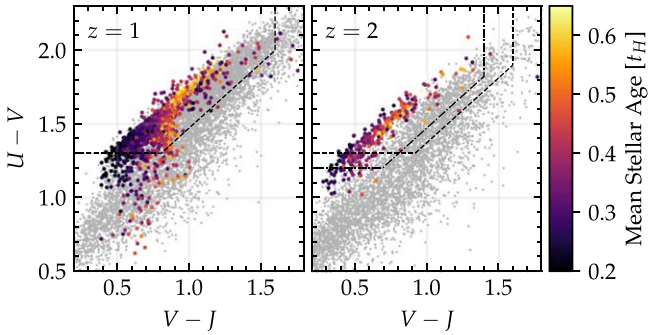

Figure 11. Gradient in stellar age for quiescent galaxies on the *UVJ* diagram. The left (right) panel shows the *UVJ* diagram at $z = 1$ ($z = 2$), and points are colored by the mass-weighted mean stellar age.

inclination (Patel et al. 2012), and this has been supported by semianalytical models (Zuckerman et al. 2021). Such variations in the star−dust geometry will lead to varying attenuation curves (Narayanan et al. 2018), and assuming a universal attenuation curve in spite of this variation will produce a stronger observational correlation between SFR and location in *UVJ* space.

In summary, while the trends we observe in sSFR on the *UVJ* diagram are subtler than observed trends, this can be largely attributed to the fact that observations tend to assume a universal attenuation curve in spite of underlying variation. A full analysis of the dependence of galaxy properties derived from SEDs on the assumed attenuation curve is beyond the scope of this paper (though it is explored in more detail in Lower et al. 2020, 2022). That said, we note that a continual trend in sSFR on the *UVJ* diagram has been reproduced even with SED fitting codes that allow for a varying attenuation curve (e.g., Leja et al. 2019).

3.2.3. Stellar Age

Finally, we examine trends in stellar age on the *UVJ* diagram. Figure 11 shows quiescent galaxies on the *UVJ* diagram at $z = 1$ and $z = 2$, with points colored by the mass-weighted mean stellar age as a fraction of the Hubble time. We compute mass-weighted mean stellar ages by averaging the

formation times of star particles, weighted by the formation masses, computed using an FSPS SSP to account for mass loss by evolved stars. We show only quiescent galaxies in Figure 11, as we do not observe a trend in stellar age for SFGs. Though this is in contrast to the observations of Whitaker et al. (2012), it is consistent with the subtlety of the trend we see with sSFR in *UVJ* space.

A clear trend in mean stellar age has been observed in the quiescent region of *UVJ* space (Whitaker et al. 2012, 2013; Belli et al. 2019). Leja et al. (2019) showed that this trend in stellar age, along with trends in metallicity, is not perfectly constrained by *UVJ* colors alone and instead is a result of more fundamental galaxy scaling relationships. Regardless, as an oft-used observable, it is a fruitful comparison to investigate trends with stellar age in *UVJ* space. We reproduce the observed gradient in stellar age reasonably well, with the oldest galaxies universally occupying the top right of the quiescent population. Furthermore, we find that the youngest quenched galaxies typically lie in the lower left of the quenched region, consistent with observations of PSB (or E+A) galaxies (e.g., Yano et al. 2016; Almaini et al. 2017; Suess et al. 2020). The age gradient in the quenched region implies a fairly universal, predictable evolution of galaxies on the *UVJ* diagram once they quench.

However, the inferred evolution of quiescent galaxies in *UVJ* space is complicated by the nontrivial portion of quenched galaxies that lie outside the quenched region, particularly at $z = 1$. These aberrant galaxies show slightly higher sSFRs than the rest of the quenched population but are generally older than we would expect based on a simple age gradient along the diagonal in Figure 11. These galaxies have bluer $U - V$ colors than galaxies in the quenched region owing to a recent frosting of star formation (e.g., Ford & Bregman 2013; Haines 2013; Akhshik et al. 2021). Indeed, $\sim 60\%$ of these galaxies have a ratio of their averaged SFRs $\mathrm{SFR}_{50}/\mathrm{SFR}_{200} > 1$, compared to $\lesssim 10\%$ for quenched galaxies in the quenched region.

4. Time Evolution in *UVJ* Space

We have shown that the SIMBA and POWDERDAY models broadly reproduce the observed *UVJ* diagram, and we have explored the factors driving inconsistencies with observations. With some confidence that our simulations reasonably reproduce observations, we now turn our attention to understanding the physics that drives the evolution of galaxies in *UVJ* space. Though much of the analysis presented thus far has focused on the flagship 100 Mpc h^{-1} SIMBA run, we now turn our attention to the higher-resolution 25 Mpc h^{-1} SIMBA run, which outputs twice as many snapshots and thus provides substantially improved time resolution. Because of the smaller box size—and hence higher mass resolution—the 25 Mpc h^{-1} box has significantly more low-mass galaxies identified than our fiducial 100 Mpc h^{-1} box. Therefore, in order to compare our results directly to the analysis presented thus far, we select only those galaxies with $\log M_*/M_\odot > 9.5$ at $z = 1$. We further limit our analysis to only those massive galaxies that are quenched by $z = 1$. We trace progenitors of these galaxies from $z \sim 2.6$ to $z = 1$ in order to study their evolution as they quench. Of the 24 galaxies in our sample of massive, quenched galaxies at $z = 1$, we find that 4 galaxies were quenched before $z \sim 2.6$ and thus do not experience a "quenching event" in the time span tracked. As our goal is to explore how galaxies evolve in color–color space as they quench, we do not include these galaxies in the subsequent analysis.

Figure 12 shows the evolution of $U - V$ and $V - J$ colors, SEDs, sSFR, and A_V for five of the galaxies tracked. In all panels, points are colored by $t - t_q$, the time since quenching. We define t_q as the time at which a galaxy first drops below $\mathrm{sSFR} = 0.2\, t_\mathrm{H}^{-1}$, where t_H is the age of the universe at that epoch (following Pacifici et al. 2016; Rodríguez Montero et al. 2019). The top row shows the *UVJ* diagram, and the second row shows attenuated SEDs at every third snapshot. The third row shows star formation histories, with solid lines indicating the relevant sSFR thresholds and dashed lines indicating the start and end times of quenching. The bottom row shows A_V as a function of time. We refer to these galaxies by their IDs, listed in the corners of the top panel in each column in Figure 12. We show the evolution of the *UVJ* colors for the remaining 16 galaxies in Figure A1.

From Figure 12, it is evident that there are a diversity of quenching pathways through the *UVJ* diagram. Some galaxies, like galaxy 2, consistently move toward the quenched region as they evolve and enter the quenched region along the diagonal section of the boundary. Others, like galaxies 6 and 17, evolve more chaotically through the blue cloud but enter the quenched region in a similar fashion. Others still enter the quenched region from the bottom left. Galaxy 108 moves upward and to the right on the *UVJ* diagram as it gets dustier, and then it moves to the left and enters the quenched region near the bottom left. Galaxy 36, in contrast, moves rapidly to the left edge of the blue cloud as it forms a burst of stars and declines in dust attenuation, entering the quenched region from the bottom left.

The diversity of quenching pathways in *UVJ* space is consistent with the diversity of SFHs we find in SIMBA and the dependence of dust attenuation on the dust geometry of the galaxy. We now further investigate the tracks that galaxies take in *UVJ* space, investigating the dependencies on quenching timescale and SFH.

4.1. Fast versus Slow Quenching

First, we explore the dependence of color–color evolution on the quenching timescale. Recent observations suggest that galaxies that quench on different timescales may trace different paths. In particular, Belli et al. (2019) explore toy models for the *UVJ* colors of fast-quenching and slow-quenching galaxies at $1.5 < z < 2.5$. They find that a fast-quenching galaxy (a tau-model SFH with a decay timescale $\tau \sim 100$ Myr) would typically enter the quenched region of *UVJ* space from the bottom left, while a slow-quenching galaxy (with $\tau \sim 1$ Gyr) would typically enter along the diagonal line, at redder colors. Similarly, Carnall et al. (2019) explore the *UVJ* evolution of massive quiescent and green valley galaxies in the VANDELS survey at $1.0 < z < 1.3$. They find a typical model track that enters the quiescent region along the diagonal line, moves to bluer colors and enters the PSB region from the top right, and then pivots to continue moving to redder colors. They find that the timing ($z_\mathrm{quench} \sim 2$ vs. $z_\mathrm{quench} \sim 1$) and the speed of quenching both affect this model track in subtle ways.

However, these models are built on simplified assumptions for both the galaxy star formation history and the dust attenuation curve. We therefore employ our cosmological simulations in order to assess the role that quenching timescale may have in the *UVJ* color evolution of redshift $z = 1$–2 galaxies. To do this, we first compute quenching times following the definition of Rodríguez Montero et al. (2019):

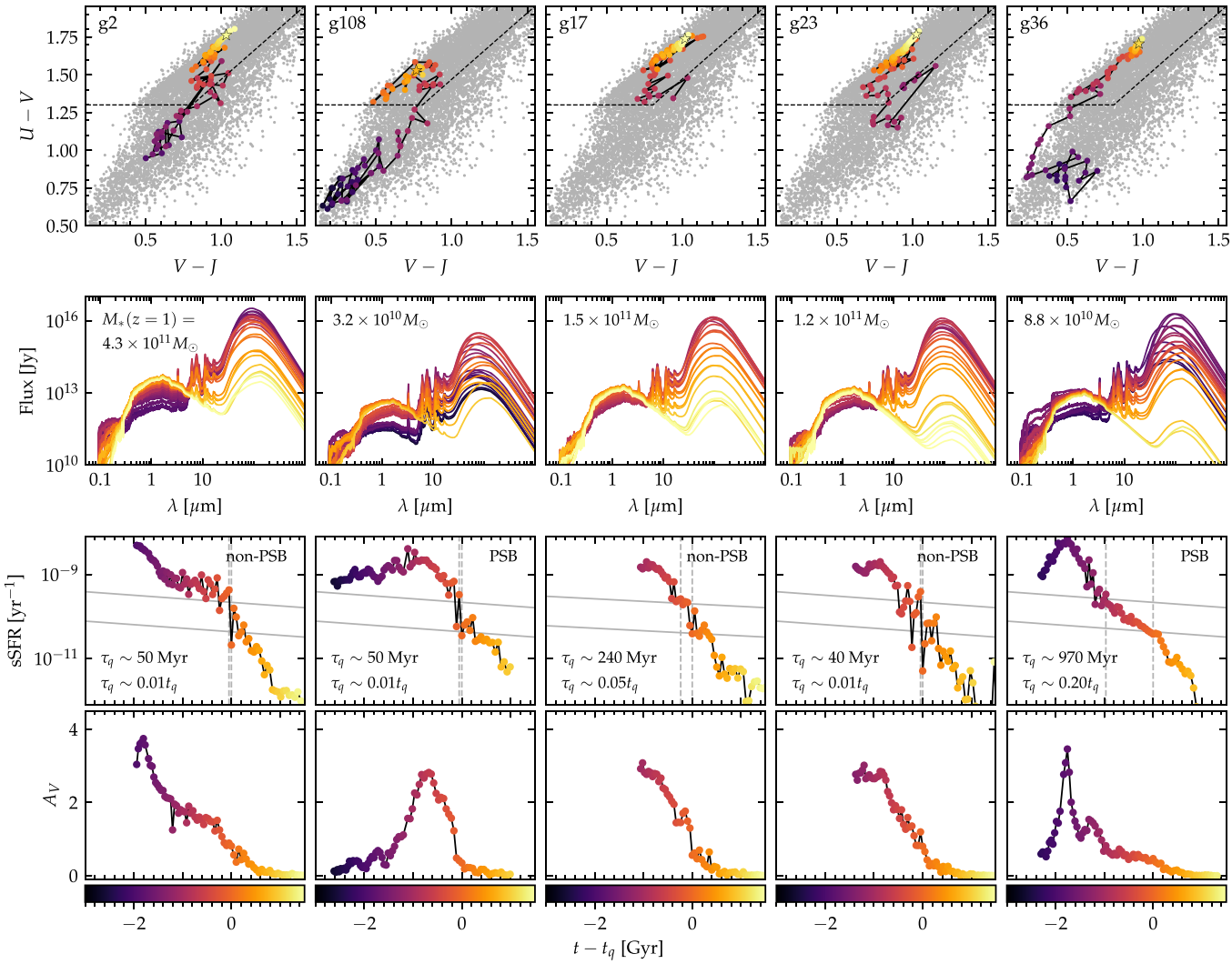

Figure 12. Evolution of *UVJ* colors from $z \sim 2.6$ to 1 for five galaxies in the process of quenching. In all panels, points are colored by time since quenching. The top row shows $U - V$ vs. $V - J$ colors for each galaxy, and the stars indicate the galaxy locations at $z = 1$. The next row shows the SEDs at every third snapshot, with the $z = 1$ stellar mass is annotated. The third row shows the sSFR, with solid lines indicating the sSFR thresholds used to define quenching times and dashed lines indicating the start and end times of quenching. We additionally categorize the galaxies as "PSB" or "non-PSB" as described in Section 4.2. The bottom row shows the dust attenuation A_V. Open circles on the time series panels indicate where galaxies are within the quenched region of *UVJ* space.

we compute the quenching timescale τ_q, in Gyr, as the time it takes the galaxy to go from the "star-forming threshold" sSFR $> t_{\rm H}^{-1}$ to the "quenched threshold" sSFR $< 0.2\, t_{\rm H}^{-1}$, where $t_{\rm H}$ is the age of the universe at that epoch. We refer to the times at which a galaxy crosses the star-forming and quenched thresholds as $t_{\rm start}$ and t_q, respectively. For a galaxy to be quenched, we additionally impose the requirement that it remain below the star-forming threshold for an additional $0.2\, t_q$ after quenching. By this definition, τ_q represents the time it takes a galaxy to cross the green valley, comparable to the distinction between fast and slow provided by Carnall et al. (2019). Rodríguez Montero et al. (2019) found that SIMBA galaxies under this definition naturally divide into "fast" ($\tau_q \sim 0.01 t_q$) and "slow" ($\tau_q \sim 0.1 t_q$) quenching modes.

Figure 13 shows how galaxy evolution in *UVJ* space depends on τ_q. We explore this question in two ways: first, by computing the median track in *UVJ* space for fast- versus slow-quenching galaxies (middle panel), and second, by computing the *UVJ* colors of each galaxy at the time of quenching t_q (right panel). The left panel of Figure 13 shows SFHs, scaled by $t_{\rm H}$ to fit the quenching thresholds and with the x-axis centered on t_q.

We compute median tracks by taking the median $U - V$ and $V - J$ colors for our sample in bins of $t - t_q$. We split our sample into fast- and slow-quenching at $\log_{10}(\tau_q/t_{\rm H}) = -1.5$, or roughly $\tau_q \approx 0.03 t_{\rm H}$. We additionally plot kernel density estimate (KDE) contours showing the distribution of fast- and slow-quenching *UVJ* colors at all time steps. These contours capture the dispersion of *UVJ* trajectories underlying the median track and are intended to highlight the diversity. It is clear from Figure 13 that there is not a distinct difference between the *UVJ* evolution of fast- and slow-quenching galaxies. In fact, if anything, slow-quenching galaxies preferentially enter the quiescent region from the bottom left, in direct conflict with what is inferred from observations. Nevertheless, despite substantial differences in τ_q, the median tracks and the *UVJ* colors at t_q do not indicate a clear preference for fast- versus slow-quenching galaxies to enter the quenched region from different locations.

The definition of τ_q as the time it takes a galaxy to cross the green valley is not the only way to assess fast versus slow quenching. In order to provide a more direct comparison to the results of Belli et al. (2019), we also fit a simple exponentially

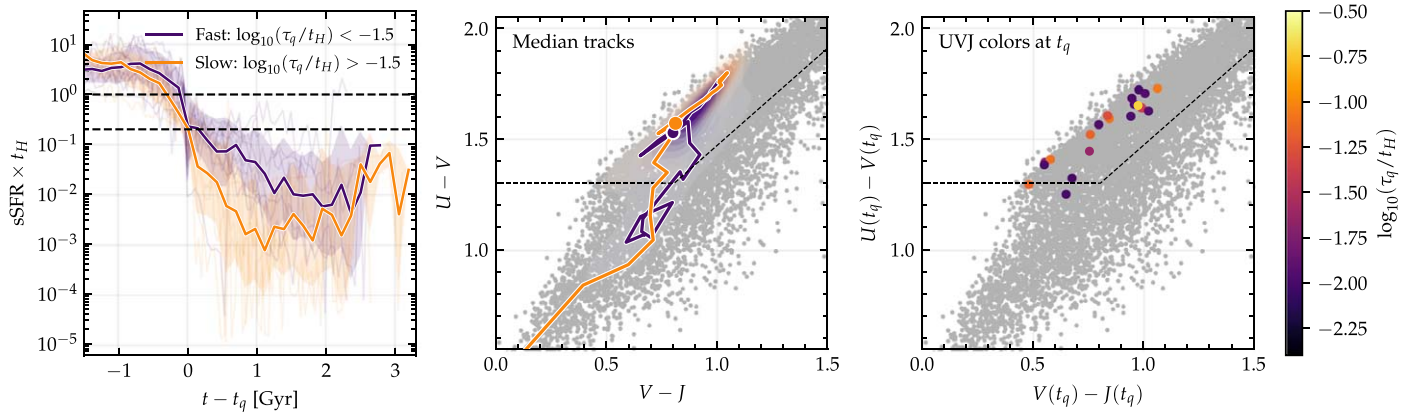

Figure 13. Evolutionary tracks in *UVJ* space as a function of the quenching timescale τ_q. Left: median SFHs for fast- and slow-quenching galaxies. The sSFR is scaled by t_H to match the definition of quenching timescale, and the x-axis is centered on the time of quenching t_q. Middle: median evolutionary tracks in *UVJ* space, in bins of $t - t_q$, for fast- and slow-quenching galaxies. Points indicate the median *UVJ* colors at $t = t_q$. We show KDE contours of the distribution of *UVJ* colors for all fast- and slow-quenching galaxies at all time steps in order to highlight the diversity underlying the median. Right: *UVJ* colors at the time of quenching, colored by the quenching timescale. We see no clear evidence for different evolutionary tracks for fast- vs. slow-quenching galaxies.

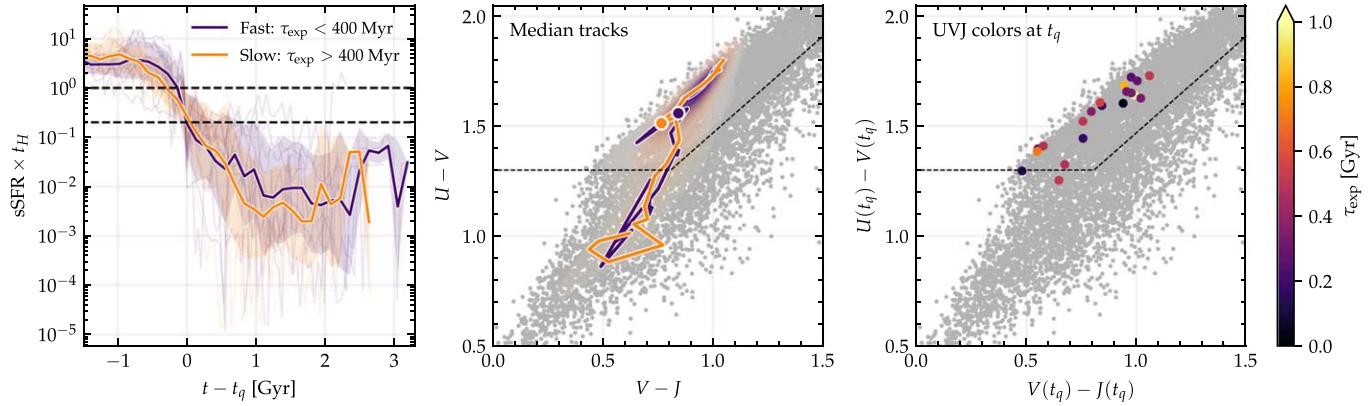

Figure 14. Evolutionary tracks in *UVJ* space as a function of the SFH decay timescale τ_{exp}. We again see no clear evidence for different evolutionary tracks for fast- vs. slow-quenching galaxies.

declining model to the SFHs of each simulated galaxy. We consider only a limited portion of each SFH, starting at the time of peak SFR prior to quenching and ending 1 Gyr after quenching. We fit a decaying exponential model using

$$\mathrm{SFR} \propto e^{-(t-t_0)/\tau_{exp}}, \quad (2)$$

where t_0 is the time of peak SFR and τ_{exp} is the decay time, the parameter to be fit.

Figure 14 shows how galaxy evolution in *UVJ* space depends on τ_{exp}. Here we split the sample into fast- and slow-quenching at $\tau_{exp} = 400$ Myr in order to correspond roughly to the 100 Myr and 1 Gyr model tracks presented by Belli et al. (2019). As with τ_q, we do not see clear evidence for distinct *UVJ* evolutionary tracks based on the quenching timescale: the median tracks are nearly identical, and galaxies with different τ_{exp} seem to enter the quenched region from similar locations. This is in distinct contrast to the results of Belli et al. (2019) and Carnall et al. (2019) and implies that the primary factors driving the evolution of *UVJ* colors in SIMBA are not strongly correlated with the quenching timescale.

4.2. Post-starburst Galaxies

Despite the lack of distinct evolutionary tracks for fast versus slow quenching, the observational evidence for the clustering of PSB galaxies in the lower left of the quenched region in *UVJ* space implies that these galaxies must follow a unique evolutionary track. We have shown that this is indeed the region where our youngest quenched galaxies tend to lie (see Figure 11).

While PSB galaxies are typically associated with fast quenching timescales, this correlation may not be universal. In the dual-origin model for PSBs presented by Wild et al. (2016), at low redshift ($z \lesssim 1$) PSBs are formed by the *rapid* quenching of normal SFGs, while at high redshift ($z \gtrsim 2$) PSBs are formed by a period of intense starburst and subsequent quenching. That is, at $2.6 \lesssim z < 1$, we may expect PSBs not to necessarily show universally rapid quenching timescales, but rather to be characterized by intense starburst prior to quenching. Therefore, we classify galaxies by computing their mean sSFR (scaled by t_H) in the 1 Gyr prior to the onset of quenching. We write this quantity as $\langle \mathrm{sSFR} \times t_H \rangle_{\text{pre-quenching}}$, or simply $\langle \mathrm{sSFR} \times t_H \rangle$. Since the sSFR can be interpreted as the inverse of the stellar mass doubling time, a value of $\langle \mathrm{sSFR} \times t_H \rangle > 5$ would indicate that the stellar mass could double in less than one-fifth of a Hubble time, or $\sim$1 Gyr at $z \sim 1$.

Figure 15 shows the evolution of *UVJ* colors as a function of $\langle \mathrm{sSFR} \times t_H \rangle$. In the left panel, we again plot the SFHs, but this time with the x-axis centered on t_{start}, the time at which quenching began, in order to highlight the 1 Gyr time span prior to quenching on which we average the sSFR. We split the

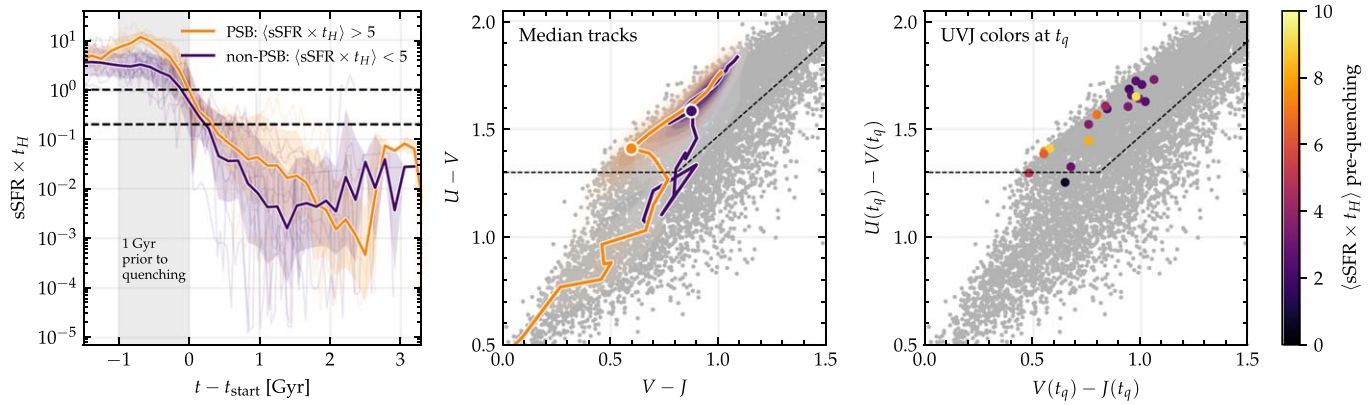

Figure 15. Evolutionary tracks in *UVJ* space as a function of the mean sSFR over the 1 Gyr prior to the onset of quenching, $\langle \mathrm{sSFR} \times t_{\mathrm{H}} \rangle$. Note that in the left panel the x-axis is now centered on t_{start}, the time at which the galaxy first leaves the star-forming threshold, and the gray shaded region indicates the 1 Gyr time span on which we average the sSFR. We see a distinct difference in the median *UVJ* evolutionary track for galaxies that quench immediately post-starburst.

sample into two groups, "PSBs" with $\langle \mathrm{sSFR} \times t_{\mathrm{H}} \rangle > 5$ and "non-PSBs" that do not satisfy this criterion. This definition yields 7 PSBs and 13 non-PSBs. The median SFHs for these two groups are distinctly different, with the PSB group showing an extreme peak in the SFH prior to quenching but taking longer to reach lower sSFRs after quenching. We also see a distinct difference in the median *UVJ* diagram tracks. PSB galaxies, which quench following a starburst, typically veer toward the quenched region early and enter from the bottom left. In contrast, non-PSB galaxies move to redder colors in the star-forming region before entering the quenched region along the diagonal boundary. While there is significant diversity in the *UVJ* evolutionary pathways underlying the median track, the PSB population shows a particularly high density just outside the quenched region on the bottom left. We can additionally see this effect in the right panel: most of the galaxies entering the quenched region from the bottom left are PSBs, while those entering from the right are not.

We see that PSBs follow a unique evolutionary pathway in *UVJ* space, but what physical mechanism causes this divergence from the non-PSB galaxies? As it turns out, PSBs are driven into this region by a rapid loss of dust as they quench. In the SIMBA model, dust can be destroyed in star formation, primarily due to astration in the hot environments near stars and, to a lesser degree, thermal sputtering in the ISM (Li et al. 2019).[16] PSBs in SIMBA thus lose most of their dust during starburst and converge on a dust-free model track in *UVJ* space earlier than non-PSB galaxies (i.e., before fully quenching). For example, we see in Figure 12 that galaxy 36 experiences a rapid drop in dust attenuation during starburst, such that it has $A_V \sim 0.5$ by the time it begins quenching. By contrast, galaxy 6, which does not experience a starburst, has $A_V \sim 1$ at the start of quenching.

Accurately assessing the rate at which dust is lost during quenching is critical in deriving *UVJ* evolutionary tracks from observations. This is typically done by assuming a relationship between the SFR and the dust attenuation A_V to model the change in colors with decreasing SFR. This is the method employed by both Belli et al. (2019) and Carnall et al. (2019), though the model tracks produced by the two authors differ significantly. This is largely because Belli et al. (2019) have no data to constrain this relationship and simply assume that A_V falls linearly with SFR as galaxies quench. By contrast, Carnall et al. (2019) fit a linear relationship between A_V and log(nSFR) for a sample of green valley galaxies.

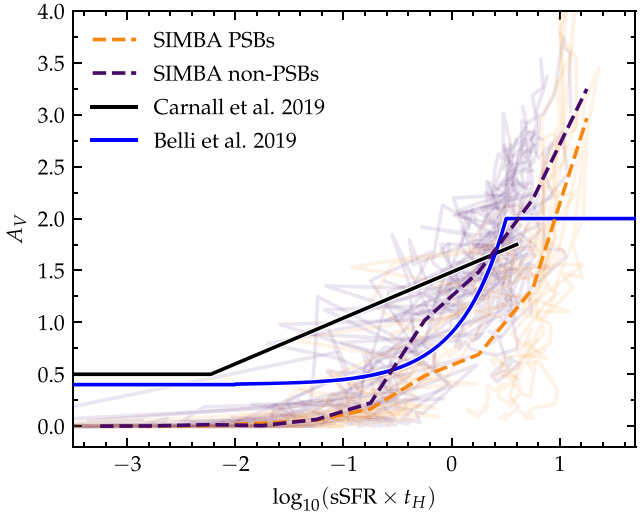

Figure 16. Dust attenuation A_V vs. $\log_{10}(\mathrm{sSFR} \times t_{\mathrm{H}})$ for SIMBA PSB galaxies (orange) and non-PSBs (purple). For both populations, we show both the median A_V in bins of $\log_{10}(\mathrm{sSFR} \times t_{\mathrm{H}})$ and tracks for individual galaxies. The solid black line shows the ansatz used by Carnall et al. (2019) to infer model tracks on the *UVJ* diagram. The solid blue line shows the ansatz used by Belli et al. (2019). Though not perfect, our results in general more closely match the Belli et al. ansatz. Furthermore, our PSB galaxies drop in A_V more quickly, or at higher sSFR, than the non-PSB population.

Figure 16 shows how these two models compare to our results for the relationship between A_V and sSFR.[17] We show the relationship between A_V and $\log(\mathrm{sSFR} \times t_{\mathrm{H}})$ for both our PSB galaxies (orange) and non-PSBs (purple). First, we see that our results more closely match the Belli et al. ansatz, where A_V drops following the SFR. Furthermore, we note that the PSB galaxies drop to lower A_V at the same sSFR than the non-PSB population. This reflects the rapid destruction of dust during

[16] Note: these simulations do not include shattering as a dust destruction process (e.g., Li et al. 2021).

[17] To plot the ansatz of Carnall et al. (2019), we convert the equation provided from log(nSFR) to $\log(\mathrm{sSFR} \times t_{\mathrm{H}})$ using a linear fit derived from SIMBA data. To plot the ansatz of Belli et al. (2019), we assume that galaxies start with $\log(\mathrm{sSFR} \times t_{\mathrm{H}}) = 0.5$ and $A_V = 2$ and that A_V scales with $\mathrm{sSFR} \times t_{\mathrm{H}}$ until settling at a constant value of $A_V = 0.4$ at $\log(\mathrm{sSFR} \times t_{\mathrm{H}}) = -2$. While differing definitions prohibit perfect comparison between these assumptions and our results, they remain useful for qualitative comparison.

starburst and is a major reason we see PSBs follow the *UVJ* pathway they do, despite not necessarily quenching rapidly.

4.3. Time Evolution Summary

These results, in general, support the interpretations of recent observations (e.g., Barro & Faber 2014; Belli et al. 2019; Carnall et al. 2019; Suess et al. 2021) that there are, to first order, two quenching pathways in *UVJ* space: one that enters the quenched region at some point along the diagonal boundary, and another that enters from the bottom left. While we do not observe a difference in *UVJ* evolution based on the quenching timescale, we do see that the latter pathway is primarily associated with PSBs.[18] However, we caution that these median tracks are indeed the median of a diverse array of *UVJ* evolutionary paths. As we show in Figure 12, two galaxies that follow similar evolution in general, or enter the quenched region in similar ways, may trace significantly different paths as they move somewhat chaotically through the blue cloud. While this may be due simply to the discreteness of our simulation snapshots and the dependence of our radiative transfer on the evolving geometry of the galaxy, we nevertheless caution that the evolution of galaxies in color–color space is sensitive to more than just SFR and A_V.

The lack of a clear relationship between the quenching timescale and the formation history of our model galaxies holds implications for observations. In fact, recent resolved HST observations of galaxies at $z \gtrsim 1$ find that galaxies that form late experience fast quenching in their centers, whereas early formation correlates with slow/uniform quenching (Akhshik et al. 2022). Thus, it may be critical to explicitly consider the quenching within the central 1 kpc when connecting quenching timescales to the global formation histories in future theoretical work.

5. Discussion: Comparison to Other Models

In this section, we compare the results of our simulations to theoretical models in the literature that have attempted to understand the observed *UVJ* diagram.

5.1. Overview

We compare to three different simulation campaigns that have studied the *UVJ* diagram in the content of galaxy evolution: Davé et al. (2017), Donnari et al. (2019), and Roebuck et al. (2019). Davé et al. (2017) and Donnari et al. (2019) employed cosmological galaxy evolution simulations (similar to those studied here), while Roebuck et al. (2019) focused on idealized galaxy models. The former papers simulated synthetic colors via LOS ray-tracing models, while Roebuck et al. (2019) used bona fide radiative transfer calculations as in our work. In what follows, we compare both the quenching models (and impact on the separation between star-forming and quenched galaxies) and the impact of assumed/modeled dust attenuation laws in these works on the modeled colors.

[18] This result—that PSBs in SIMBA do not necessarily quench rapidly, but do follow the PSB evolutionary track inferred from observations—may explain why we observe an overdensity of transition galaxies just outside the quenched region on the bottom left: PSBs in SIMBA quench slowly relative to observations and spend more time in this transition region.

5.2. Galaxy Quenching Models

Critical to computational studies of galaxy quenching is the underlying physical model responsible for quenching massive galaxies. In recent years, an AGN-driven scenario for quenching in massive galaxies has gained traction (see, e.g., Dubois et al. 2013). Indeed, the inclusion of AGN feedback in SIMBA is one of the major differences between it and its predecessor simulation, MUFASA (Davé et al. 2016). While MUFASA used a phenomenological model for quenching, which prevents gas from cooling onto galaxies in halos above a certain redshift-evolving halo mass threshold, SIMBA allows galaxies to quench naturally based on subgrid models for black hole feedback. Davé et al. (2019) show that these models for AGN feedback are primarily responsible for quenching massive galaxies, with jet-mode feedback dominating but X-ray feedback playing a subtle but important role.

The quenching model used in IllustrisTNG is broadly similar to SIMBA, in which quenching is driven primarily by kinetic AGN feedback. That said, there are some key differences in the two models. In particular, SIMBA does not vary the direction of AGN jets as IllustrisTNG does. Additionally, SIMBA employs bipolar kinetic AGN feedback at all Eddington ratios, while IllustrisTNG employs spherical thermal feedback at high ratios and kinetic feedback at low ratios. The differences between the SIMBA an IllustrisTNG AGN feedback implementations, while subtle, have been shown to play a role in determining the cold gas content of SFGs, particularly at high redshift (Davé et al. 2020).

The slight overpopulation of the green valley in SIMBA (which contributes to the lack of a clear *UVJ* bimodality) is dominated by galaxies with $10 < \log M_*/M_\odot < 11$ (Davé et al. 2019, their Figure 6). In contrast, the distribution of galaxy SFRs in TNG does not show overpopulation of the green valley in this same mass range (Donnari et al. 2019, their Figure 8). These differences in the distribution of SFRs between the two simulations are likely driven by differences in the feedback implementations. In particular, TNG feedback randomizes the jet direction and is able to expel the ISM in the low-$f_{\rm edd}$ mode. In contrast, SIMBA assumes bipolar jets that are decoupled until beyond the ISM. This is likely an important reason why IllustrisTNG produces a clear color bimodality on the *UVJ* diagram whereas SIMBA does not.

5.3. Dust Attenuation Models

The treatments of dust in the models of Davé et al. (2017), Donnari et al. (2019), and Roebuck et al. (2019) all differ from each other and from this work in key ways. Davé et al. (2017) derive a dust attenuation curve for each galaxy using the ray-tracing package LOSER,[19] which acts as a computationally inexpensive alternative to dust radiative transfer. They use a redshift-dependent dust-to-metals ratio and a Cardelli et al. (1989) Milky Way extinction law.[20] Meanwhile, the dust model used by Donnari et al. (2019; described in detail in Nelson et al. 2018) includes the empirical model of Charlot & Fall (2000) and additionally models dust scattering analytically following Calzetti et al. (1994) and dust absorption following Cardelli et al. (1989) with a redshift- and metallicity-dependent dust-to-gas ratio. Finally, Roebuck et al. (2019) use idealized simulations and radiative transfer to determine galaxy colors,

[19] https://pyloser.readthedocs.io/en/latest/

[20] PYLOSER is now included by default in CAESAR.

though they assume a constant dust-to-metals ratio of 0.4 (as opposed to our on-the-fly model for dust evolution from Li et al. 2019).

A major difference between the models used in this work and those used by Davé et al. (2017) and Donnari et al. (2019) is the use of dust radiative transfer versus LOS extinction. The inclusion of full 3D dust radiative transfer is important in capturing the variation of the dust attenuation curve, and, indeed, Roebuck et al. (2019) also find significant variation in the attenuation curve that drives galaxy locations in *UVJ* space. This is likely a significant reason that our models produce a larger spread of *UVJ* colors for SFGs—including populating the dusty star-forming region—than those of Davé et al. (2017) or Donnari et al. (2019), which generally employ attenuation curves with fixed shapes.

Notably, while our model succeeds in reproducing the observed population of highly dust-reddened galaxies, there remain tensions with observations. In particular, as discussed in Section 3.2.1, the attenuation curve shapes of our model galaxies differ from the typically assumed Calzetti et al. (2000) curve, and this difference is more significant at higher masses. We attribute this to the increasingly complex star−dust geometry in higher-mass galaxies, which may be related to the quenching model. As dust in SIMBA is advected passively with gas elements, the star−dust geometry would be impacted by any process that alters the spatial distribution of the gas. The AGN feedback model in SIMBA does just that: Borrow et al. (2020) show that jet-mode AGN feedback is capable of transferring galaxy baryons great distances, in some cases several megaparsecs. Therefore, while the radiative transfer models employed in this work are certainly more robust than LOS extinction models, they are dependent on the somewhat unconstrained evolution of the 3D distribution of gas at the epoch of quenching. Recent simulations such as those performed by Li et al. (2021), which decouple gas and dust, may help to address this issue.

6. Conclusions

In this work, we have studied the evolution of galaxies on the *UVJ* diagram using the SIMBA simulations and POWDERDAY 3D dust radiative transfer. Our main conclusions are summarized as follows:

1. The SIMBA dust model in combination with POWDERDAY dust radiative transfer broadly reproduces the observed distribution of galaxies on the *UVJ* diagram at $z = 2$ and $z = 1$. In particular, we reproduce:
   (a) the clustering of galaxies into star-forming and quiescent regions;
   (b) the relationship between $V - J$ color and A_V for SFGs, including the population of extremely dust-reddened galaxies at the top right of the diagram;
   (c) the diagonal gradient in stellar age for quiescent galaxies.
2. However, we fail to reproduce observations in several key ways:
   (a) We do not reproduce a clear bimodality in the number density of galaxies in *UVJ* space, likely due to the overpopulation of the green valley in SIMBA and the dust attenuation curve shapes.
   (b) We populate the dusty star-forming region primarily with low-mass ($\log M_*/M_\odot < 10.5$) rather than higher-mass galaxies. These low-mass, high-A_V galaxies are not typically found in observational surveys and may be due to issues with the SIMBA dust evolution model.
3. We find that the assumption of a universal, Calzetti et al. (2000) dust attenuation law can lead to bias in the inferred SFRs in the star-forming region of *UVJ* space, with SFGs near the quiescent region having their SFRs underestimated by as much as 0.5 dex. We caution that trends in *UVJ* space may be exaggerated by the assumption of a universal attenuation law.
4. In contrast to what is typically inferred from observations, we find little correlation between the quenching timescale and the pathway a galaxy follows in *UVJ* space as it quenches. Instead, we show that the evolution of galaxies in *UVJ* space is driven primarily by the intensity of its star formation in the 1 Gyr prior to the onset of quenching. Galaxies that experience a burst of star formation prior to quenching veer to the left edge of the blue cloud and enter the quenched region from the bottom left. Galaxies that do not experience such a burst in star formation enter the quenched region along the diagonal boundary.

Interpretation of our results is limited by the extent to which we fail to reproduce the observed distribution of galaxies in *UVJ* space. The fact that simulations—even those employing an explicit dust model and 3D radiative transfer—still cannot perfectly reproduce observations of color–color diagrams at high redshift highlights the need for further work modeling the relationship between dust attenuation, star formation, and morphological transition for galaxies in the process of quenching. Central to these questions is the relationship between dust geometry and the dust attenuation law (see Narayanan et al. 2018), the evolution of galactic dust during quenching (see Whitaker et al. 2021), and the morphological evolution of galaxies during quenching. Future advancements in galaxy dust modeling (e.g., Li et al. 2021) will allow us to more rigorously explore the evolution of dust properties, and such analysis will be key for improving our interpretation of observable properties of high-redshift galaxies.

This work was supported by NSF under grant AST-1908137 and REU-1851954. H.B.A. acknowledges the consistent feedback and support provided by the faculty mentors and fellow students involved in the 2020 University of Florida REU program. K.E.W. wishes to acknowledge funding from the Alfred P. Sloan Foundation. R.F. acknowledges financial support from the Swiss National Science Foundation (grant No. 194814). This work was initiated at the Aspen Center for Physics, which is supported by NSF grant PHY-1607611. Much of this work was conducted on the ancestral land of the Meskwaki, Sauk, and Ioway Peoples.

Software: PYTHON, NUMPY (van der Walt et al. 2011), MATPLOTLIB (Hunter 2007), POWERDERDAY (Narayanan et al. 2021), YT (Turk et al. 2011), HYPERION (Robitaille 2011), FSPS (Conroy & Gunn 2010; Conroy et al. 2010), GIZMO (Hopkins 2015).

Appendix A
UVJ Colors over Time for the Full Sample

Figure A1 shows the evolution of UVJ colors from z ~ 2.6 to 1 for the remaining galaxies in our sample, not pictured in Figure 12.

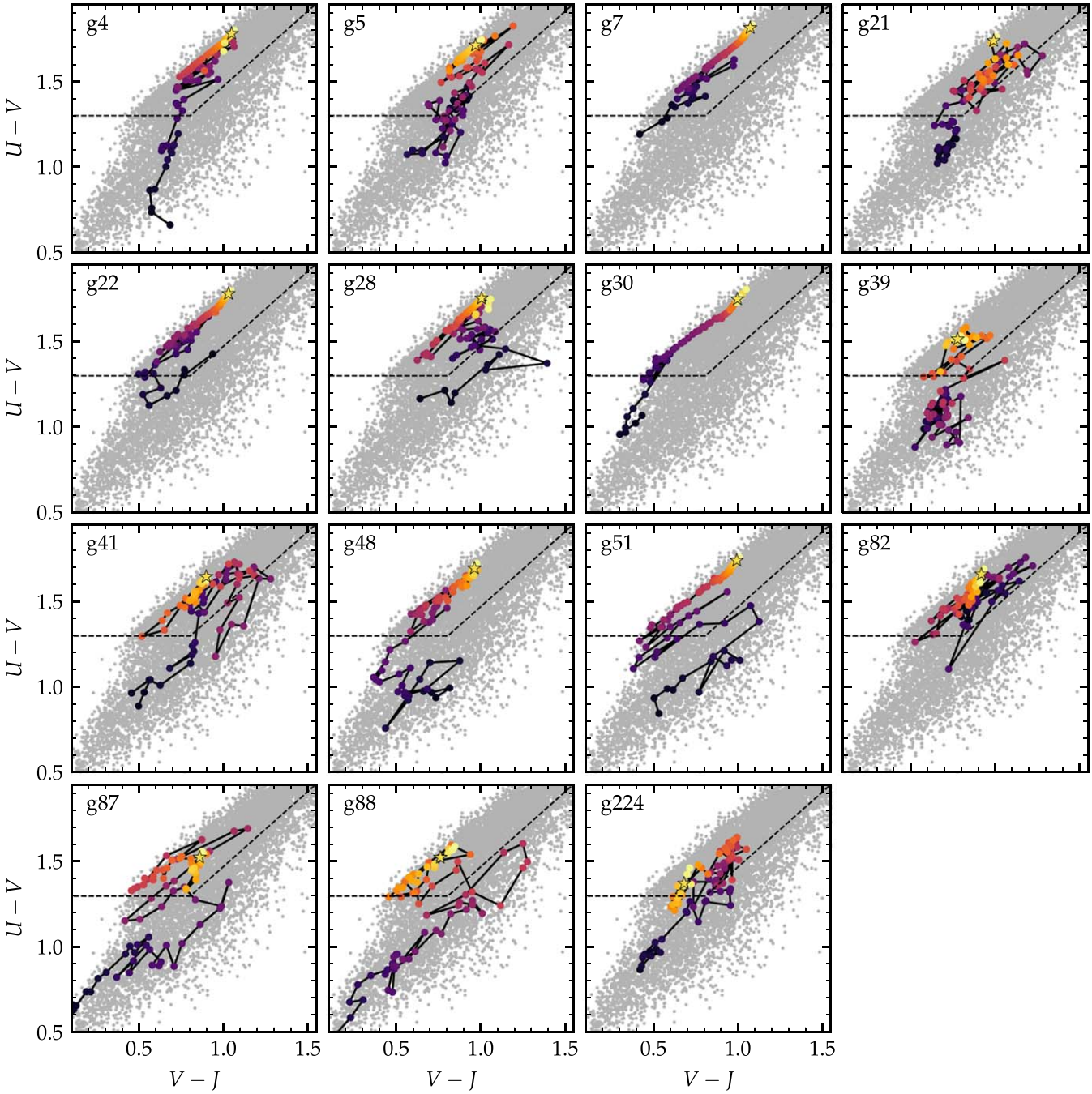

Figure A1. Evolution of *UVJ* colors from $z \sim 2.6$ to 1 for the rest of the galaxies in our sample, not pictured in Figure 12. Points are colored according to the age of the universe at that redshift, from 2.4 to 6.3 Gyr. The dashed line shows the Williams et al. (2009) *UVJ* selection criteria.

Appendix B
Mock Observational Noise

Figure B1 shows the SIMBA+POWDERDAY model *UVJ* diagram both with and without the inclusion of mock observational noise. We simulate the observational noise in the form of uncertainty in the redshift, e.g., from photometric redshift measurements in large surveys. Specifically, we apply an uncertainty of $\sigma_z/(1+z) = 0.05$ for "red" galaxies (with $U - V > 1.3$) and $\sigma_z(1+z) = 0.025$ for "blue" galaxies (with $U - V < 1.3$). We randomly select $z_{\rm phot}$ from a normal distribution Norm(2, σ_z) and calculate the rest-frame magnitudes from the shifted SED, assuming $z_{\rm phot}$. We apply an increased uncertainty for red versus blue galaxies following Whitaker et al. (2011, Figure 21).

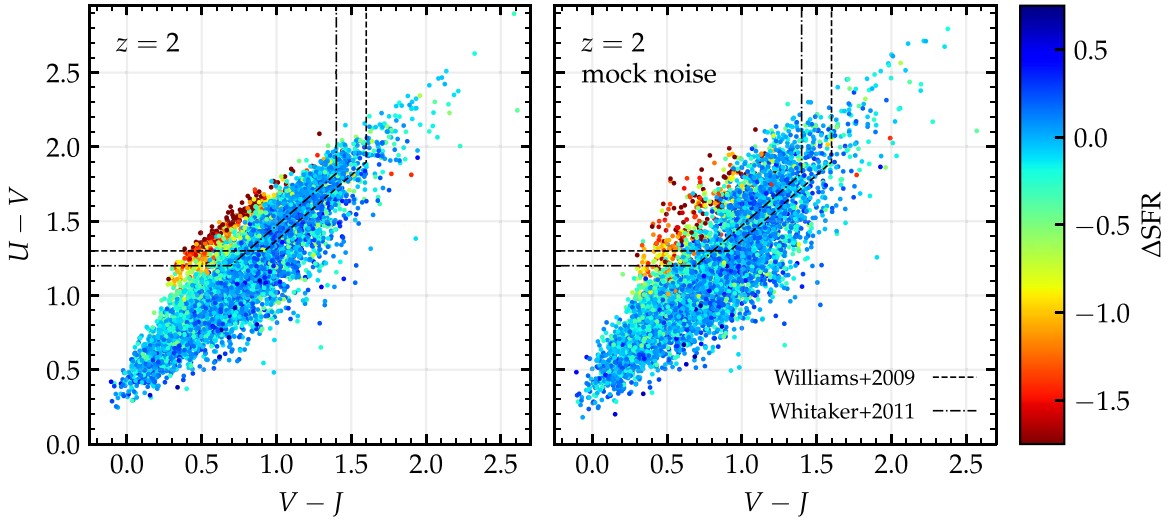

Figure B1. The *UVJ* diagram at $z = 2$, both with (right) and without (left) the addition of mock observational noise. Points are colored by ΔSFR.

ORCID iDs

Hollis B. Akins https://orcid.org/0000-0003-3596-8794
Desika Narayanan https://orcid.org/0000-0002-7064-4309
Katherine E. Whitaker https://orcid.org/0000-0001-7160-3632
Romeel Davé https://orcid.org/0000-0003-2842-9434
Sidney Lower https://orcid.org/0000-0003-4422-8595
Rachel Bezanson https://orcid.org/0000-0001-5063-8254
Robert Feldmann https://orcid.org/0000-0002-1109-1919
Mariska Kriek https://orcid.org/0000-0002-7613-9872

References

Akhshik, M., Whitaker, K. E., Leja, J., et al. 2021, ApJL, 907, L8
Akhshik, M., Whitaker, K. E., Leja, J., et al. 2022, arXiv:2203.04979
Almaini, O., Wild, V., Maltby, D. T., et al. 2017, MNRAS, 472, 1401
Anglés-Alcázar, D., Davé, R., Faucher-Giguère, C.-A., Özel, F., & Hopkins, P. F. 2017a, MNRAS, 464, 2840
Anglés-Alcázar, D., Faucher-Giguère, C.-A., Kereš, D., et al. 2017b, MNRAS, 470, 4698
Anglés-Alcázar, D., Özel, F., & Davé, R. 2013, ApJ, 770, 5
Anglés-Alcázar, D., Özel, F., Davé, R., et al. 2015, ApJ, 800, 127
Arnouts, S., Walcher, C. J., Le Fèvre, O., et al. 2007, A&A, 476, 137
Baldry, I. K., Glazebrook, K., Brinkmann, J., et al. 2004, ApJ, 600, 681
Balogh, M. L., Baldry, I. K., Nichol, R., et al. 2004, ApJL, 615, L101
Barro, G., Faber, S. M., Pérez-González, P. G., et al. 2014, ApJ, 791, 52
Bell, E. F., Wolf, C., Meisenheimer, K., et al. 2004, ApJ, 608, 752
Belli, S., Newman, A. B., & Ellis, R. S. 2019, ApJ, 874, 17
Bertelli, G., Bressan, A., Chiosi, C., Fagotto, F., & Nasi, E. 1994, A&AS, 106, 275
Bessell, M. S. 1990, PASP, 102, 1181
Bondi, H. 1952, MNRAS, 112, 195
Borrow, J., Anglés-Alcázar,, D., Davé, R., et al. 2020, MNRAS, 491, 6102
Brammer, G. B., van Dokkum, P. G., Franx, M., et al. 2012, ApJS, 200, 13
Brammer, G. B., Whitaker, K. E., van Dokkum, P. G., et al. 2009, ApJL, 706, L173
Byler, N., Dalcanton, J. J., Conroy, C., et al. 2018, ApJ, 863, 14
Byler, N., Dalcanton, J. J., Conroy, C., et al. 2019, AJ, 158, 2
Byler, N., Dalcanton, J. J., Conroy, C., & Johnson, B. D. 2017, ApJ, 840, 44
Calzetti, D., Armus, L., Bohlin, R. C., et al. 2000, ApJ, 533, 682
Calzetti, D., Kinney, A. L., Storchi-Bergmann, T, et al. 1994, ApJ, 429, 582
Cardelli, J. A., Clayton, G. C., & Mathis, J. S. 1989, ApJ, 345, 245
Carnall, A. C., McLure, R. J., Dunlop, J. S., & Davé, R. 2018, MNRAS, 480, 4379
Carnall, A. C., McLure, R. J., Dunlop, J. S., et al. 2019, MNRAS, 490, 417
Carnall, A. C., Walker, S., McLure, R. J., et al. 2020, MNRAS, 496, 695
Chabrier, G. 2003, PASP, 115, 763
Charlot, S., & Fall, S. M. 2000, ApJ, 539, 718
Choi, J., Dotter, A., Conroy, C., et al. 2016, ApJ, 823, 102
Conroy, C., & Gunn, J. E. 2010, ApJ, 712, 833
Conroy, C., White, M., & Gunn, J. E. 2010, ApJ, 708, 58
Daddi, E., Cimatti, A., Renzini, A., et al. 2004, ApJ, 617, 746
Davé, R., Anglés-Alcázar, D., Narayanan, D., et al. 2019, MNRAS, 486, 2827
Davé, R., Crain, R. A., Stevens, A. R. H., et al. 2020, MNRAS, 497, 146
Davé, R., Rafieferantsoa, M. H., & Thompson, R. J. 2017, MNRAS, 471, 1671
Davé, R., Thompson, R., & Hopkins, P. F. 2016, MNRAS, 462, 3265
Donnari, M., Pillepich, A., Nelson, D., et al. 2019, MNRAS, 485, 4817
Dotter, A. 2016, ApJS, 222, 8
Dubois, Y., Gavazzi, R., Peirani, S., & Silk, J. 2013, MNRAS, 433, 3297
Dudzevičiūtė, U., Smail, I., Swinbank, A. M., et al. 2021, MNRAS, 500, 942
Dwek, E. 1998, ApJ, 501, 643
Eldridge, J. J., Stanway, E. R., Xiao, L., et al. 2017, PASA, 34, e058
Faber, S. M., Willmer, C. N. A., Wolf, C., et al. 2007, ApJ, 665, 265
Fang, J. J., Faber, S. M., Koo, D. C., et al. 2018, ApJ, 858, 100
Feldmann, R., Quataert, E., Hopkins, P. F., Faucher-Giguère, C.-A., & Kereš, D. 2017, MNRAS, 470, 1050
Ford, H. A., & Bregman, J. N. 2013, ApJ, 770, 137
Forrest, B., Annunziatella, M., Wilson, G., et al. 2020, ApJL, 890, L1
Forrest, B., Tran, K.-V. H., Tomczak, A. R., et al. 2016, ApJL, 818, L26
Garg, P., Narayanan, D., Byler, N., et al. 2022, ApJ, 926, 80
Girardi, L., Bressan, A., Bertelli, G., & Chiosi, C. 2000, A&AS, 141, 371
Glazebrook, K., Schreiber, C., Labbé, I., et al. 2017, Natur, 544, 71
Haines, T. 2013, M.S, University of Missouri—Kansas City
Heckman, T. M., & Best, P. N. 2014, ARA&A, 52, 589
Hewett, P. C., Warren, S. J., Leggett, S. K., & Hodgkin, S. T. 2006, MNRAS, 367, 454
Hopkins, P. F. 2015, MNRAS, 450, 53
Hopkins, P. F., Kereš, D., Oñorbe, J., et al. 2014, MNRAS, 445, 581
Hopkins, P. F., & Quataert, E. 2011, MNRAS, 415, 1027
Hunter, J. D. 2007, CSE, 9, 90
Ilbert, O., McCracken, H. J., Le Fèvre, O., et al. 2013, A&A, 556, A55
Kauffmann, G., Heckman, T. M., White, S. D. M., et al. 2003, MNRAS, 341, 33
Kennicutt, R. C., Jr. 1998, ApJ, 498, 541
Kriek, M., & Conroy, C. 2013, ApJL, 775, L16
Kriek, M., Shapley, A. E., Reddy, N. A., et al. 2015, ApJS, 218, 15
Kroupa, P. 2002, Sci, 295, 82
Krumholz, M. R., & Gnedin, N. Y. 2011, ApJ, 729, 36
Labbé, I., Huang, J., Franx, M., et al. 2005, ApJL, 624, L81
Lagos, C. d. P., da Cunha, E., Robotham, A. S. G., et al. 2020, MNRAS, 499, 1948
Leja, J., Johnson, B. D., Conroy, C., van Dokkum, P. G., & Byler, N. 2017, ApJ, 837, 170
Leja, J., Tacchella, S., & Conroy, C. 2019, ApJL, 880, L9
Li, Q., Narayanan, D., & Davé, R. 2019, MNRAS, 490, 1425
Li, Q., Narayanan, D., Torrey, P., Davé, R., & Vogelsberger, M. 2021, MNRAS, 507, 548
Lovell, C. C., Geach, J. E., Davé, R., Narayanan, D., & Li, Q. 2021, MNRAS, 502, 772
Lower, S., Narayanan, D., Leja, J., et al. 2020, ApJ, 904, 33

Lower, S., Narayanan, D., Leja, J., et al. 2022, arXiv:2203.00074
Maller, A. H., Berlind, A. A., Blanton, M. R., & Hogg, D. W. 2009, ApJ, 691, 394
Marigo, P., Girardi, L., Bressan, A., et al. 2008, A&A, 482, 883
Martis, N. S., Marchesini, D., Brammer, G. B., et al. 2016, ApJL, 827, L25
McKinnon, R., Torrey, P., & Vogelsberger, M. 2016, MNRAS, 457, 3775
McLure, R. J., Dunlop, J. S., Cullen, F., et al. 2018, MNRAS, 476, 3991
Momcheva, I. G., Brammer, G. B., Brammer, P. G., et al. 2016, ApJS, 225, 27
Muzzin, A., Marchesini, D., Stefanon, M., et al. 2013, ApJ, 777, 18
Narayanan, D., Conroy, C., Davé, R., Johnson, B. D., & Popping, G. 2018a, ApJ, 869, 70
Narayanan, D., Davé, R., Johnson, B. D., et al. 2018b, MNRAS, 474, 1718
Narayanan, D., Turk, M. J., Robitaille, T., et al. 2021, ApJS, 252, 12
Nelson, D., Pillepich, A., Springel, V., et al. 2018, MNRAS, 475, 624
Nelson, E. J., Tacchella, S., Diemer, B., et al. 2021, MNRAS, 508, 219
Nenkova, M., Sirocky, M. M., Ivezić, Ž., & Elitzur, M. 2008a, ApJ, 685, 147
Nenkova, M., Sirocky, M. M., Nikutta, R., Ivezić, Ž., & Elitzur, M. 2008b, ApJ, 685, 160
Pacifici, C., Kassin, S. A., Weiner, B. J., et al. 2016, ApJ, 832, 79
Patel, S. G., Holden, B. P., Kelson, D. D., et al. 2012, ApJL, 748, L27
Patel, S. G., Kelson, D. D., Holden, B. P., Franx, M., & Illingworth, G. D. 2011, ApJ, 735, 53
Paxton, B., Bildsten, L., Dotter, A., et al. 2011, ApJS, 192, 3
Péroux, C., & Howk, J. C. 2020, ARA&A, 58, 363
Planck Collaboration, Ade, P. A. R., Aghanim, N., et al. 2016, A&A, 594, A13
Price, S. H., Kriek, M., Brammer, G. B., et al. 2014, ApJ, 788, 86
Reddy, N. A., Oesch, P. A., Bouwens, R. J., et al. 2018, ApJ, 853, 56
Robitaille, T. P. 2011, A&A, 536, A79
Rodríguez Montero, F., Davé, R., Wild, V., Anglés-Alcázar, D., & Narayanan, D. 2019, MNRAS, 490, 2139
Roebuck, E., Sajina, A., Hayward, C. C., et al. 2019, ApJ, 881, 18
Salim, S., Boquien, M., & Lee, J. C. 2018, ApJ, 859, 11
Salim, S., & Narayanan, D. 2020, ARA&A, 58, 529
Salmon, B., Papovich, C., Long, J., et al. 2016, ApJ, 827, 20
Salpeter, E. E. 1955, ApJ, 121, 161
Sánchez-Blázquez, P., Peletier, R. F., Jiménez-Vicente, J., et al. 2006, MNRAS, 371, 703
Schmidt, M. 1959, ApJ, 129, 243
Schreiber, C., Glazebrook, K., Nanayakkara, T., et al. 2018, A&A, 618, A85
Scoville, N., Faisst, A., Capak, P., et al. 2015, ApJ, 800, 108
Seon, K.-I., & Draine, B. T. 2016, ApJ, 833, 201
Shapley, A. E., Cullen, F., Dunlop, J. S., et al. 2020, ApJL, 903, L16
Skelton, R. E., Whitaker, K. E., Momcheva, I. G., et al. 2014, ApJS, 214, 24
Smith, B. D., Bryan, G. L., Glover, S. C. O., et al. 2017, MNRAS, 466, 2217
Speagle, J. S., Steinhardt, C. L., Capak, P. L., & Silverman, J. D. 2014, ApJS, 214, 15
Springel, V. 2005, MNRAS, 364, 1105
Strateva, I., Ivezić, Ž., Knapp, G. R., et al. 2001, AJ, 122, 1861
Suess, K. A., Kriek, M., Price, S. H., & Barro, G. 2020, ApJL, 899, L26
Suess, K. A., Kriek, M., Price, S. H., & Barro, G. 2021, ApJ, 915, 87
Tomczak, A. R., Quadri, R. F., Tran, K.-V. H., et al. 2014, ApJ, 783, 85
Trayford, J. W., Lagos, C. d. P., Robotham, A. S. G., & Obreschkow, D. 2020, MNRAS, 491, 3937
Tsai, J. C., & Mathews, W. G. 1995, ApJ, 448, 84
Turk, M. J., Smith, B. D., Oishi, J. S., et al. 2011, ApJS, 192, 9
Valentino, F., Tanaka, M., Davidzon, I., et al. 2020, ApJ, 889, 93
van der Walt, S., Colbert, S. C., & Varoquaux, G. 2011, CSE, 13, 22
Villaume, A., Conroy, C., & Johnson, B. D. 2015, ApJ, 806, 82
Westera, P., Lejeune, T., Buser, R., Cuisinier, F., & Bruzual, G. 2002, A&A, 381, 524
Whitaker, K. E., Franx, M., Leja, J., et al. 2014, ApJ, 795, 104
Whitaker, K. E., Kriek, M., van Dokkum, P. G., et al. 2012, ApJ, 745, 179
Whitaker, K. E., Labbé, I., van Dokkum, P. G., et al. 2011, ApJ, 735, 86
Whitaker, K. E., Narayanan, D., Williams, C. C., et al. 2021, ApJL, 922, L30
Whitaker, K. E., van Dokkum, P. G., Brammer, G., et al. 2010, ApJ, 719, 1715
Whitaker, K. E., van Dokkum, P. G., Brammer, G., et al. 2013, ApJL, 770, L39
Wild, V., Almaini, O., Dunlop, J., et al. 2016, MNRAS, 463, 832
Williams, R. J., Quadri, R. F., Franx, M., van Dokkum, P., & Labbé, I. 2009, ApJ, 691, 1879
Williams, R. J., Quadri, R. F., Franx, M., et al. 2010, ApJ, 713, 738
Wu, P.-F., van der Wel, A., Bezanson, R., et al. 2018, ApJ, 868, 37
Wuyts, S., Labbé, I., Franx, M., et al. 2007, ApJ, 655, 51
Yano, M., Kriek, M., van der Wel, A., & Whitaker, K. E. 2016, ApJL, 817, L21
Zuckerman, L., Belli, S., Leja, J., & Tacchella, S. 2021, ApJL, 922, 32